R2DET: EXPLORING RELAXED ROTATION EQUIVARIANCE IN 2D OBJECT DETECTION

Anonymous authors
Paper under double-blind review

ABSTRACT

Introducing Group Equivariant Convolution (GConv) empowers models to explore underlying symmetries hidden in visual data by sharing the filter weights after group transformations but without additional training data, improving their performance. However, in real-world scenarios, objects or scenes often exhibit perturbations of a symmetric system, specifically a deviation from a symmetric architecture, which can be characterized by a non-trivial action of a symmetry group, known as Symmetry-Breaking. Traditional GConv-based methods are limited by strict operation rules under group space, only assuming data remains strict equivariant under limited group transformations, making it difficult to adapt to Symmetry-Breaking or non-rigid transformations. Motivated by this, we mainly focus on a common scenario: rotational Symmetry-Breaking. By relaxing strict group transformations within Strict Rotation-Equivariant group $\mathbf{C}_n$, we redefine a Relaxed Rotation-Equivariant group $\mathbf{R}_n$ and introduce a novel Relaxed Rotation-Equivariant GConv (R2GConv) with only a minimal increase of $4n$ parameters compared to GConv. Based on R2GConv, we propose a Relaxed Rotation-Equivariant Network (R2Net) as the backbone and develop a Relaxed Rotation-Equivariant Object Detector (R2Det) for 2D object detection built upon it. Experimental results demonstrate the effectiveness of our R2GConv in natural image classification, and R2Det achieves excellent performance in 2D object detection with improved generalization capabilities and robustness.

1 INTRODUCTION

2D Object detection is a crucial computer vision task with applications in various domains, including autonomous driving and geosciences (Zou et al., 2023; Kaur & Singh, 2023). Recent advancements in Deep Neural Networks (DNNs) (Hussain, 2023; Huang et al., 2017; Zagoruyko & Komodakis, 2016; Xie et al., 2017) have achieved remarkable progress. Nevertheless, objects within natural images often exhibit rotation and scale variations, requiring DNNs to handle geometric transformations more flexibly. One effective approach to address this issue is data augmentation, which improves object detection performance by rotating the dataset to expand additional data volume. Still, it leads to a considerable memory and training cost. Equivariant prior-based Neural Networks (ENNs) (Gerken et al., 2023), which further incorporate symmetries and focus on the underlying physics, e.g., Strict Rotation-Equivariance (`SRE`) introduced in Group Equivariant Convolution (GConv) (Cohen & Welling, 2016a), have significantly enhanced feature learning ability and boosted downstream task performance compared to traditional detectors (Han et al., 2021). However, these ENNs merely or by default assume uniform strict symmetry across all features. But also, real-world data rarely conforms to strict symmetry. Therefore, a critical question may arise: ***do the existing ENNs appropriately incorporate prior knowledge of equivariance in the real-world context of 2D object detection or other computer vision tasks?***

This work mainly focuses on a ***common equivariance***: Rotation-Equivariance. More formally, our focus is deemed rotation-equivariant since rotating the input should be anticipated to induce an equivalent rotation in the output. Let $f(\cdot)$ denote the rotation-equivariant function for a rotational transformation $g(\cdot)$; it is known that the rotation-equivariant functions preserve the symmetry of their input, and we have $f(g(\cdot)) = g(f(\cdot))$. Using symmetry as an inductive bias in machine learning has emerged as a powerful tool, with significant conceptual and practical breakthroughs (Bronstein et al., 2021). ***Yet, a wide range of learning tasks necessitates rotational Symmetry-Breaking (Smidt***

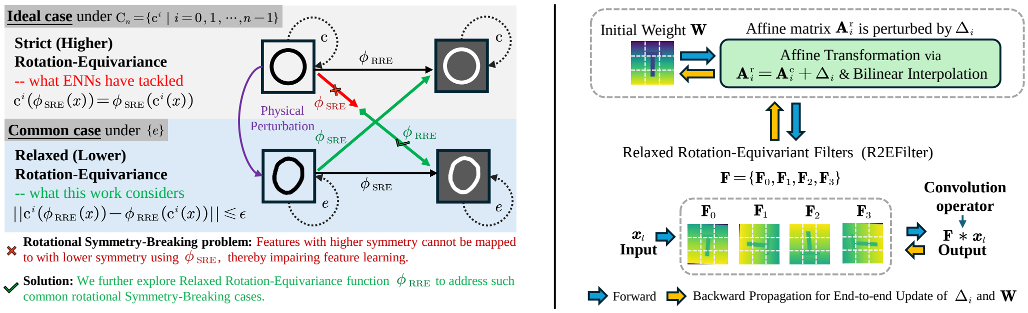
Ideal case under $C_n = \{c^i \mid i = 0, 1, \cdots, n-1\}$
Strict (Higher) Rotation-Equivariance
-- what ENNs have tackled
$c^i(\phi_{\mathrm{SRE}}(x)) = \phi_{\mathrm{SRE}}(c^i(x))$
Common case under $\{e\}$
Relaxed (Lower) Rotation-Equivariance
-- what this work considers
$\|c^i(\phi_{\mathrm{RRE}}(x)) - \phi_{\mathrm{RRE}}(c^i(x))\| \leq \epsilon$
Physical Perturbation
c
e
ϕ_{RRE}
ϕ_{SRE}
Rotational Symmetry-Breaking problem: Features with higher symmetry cannot be mapped to with lower symmetry using ϕ_{SRE}, thereby impairing feature learning.
Solution: We further explore Relaxed Rotation-Equivariance function ϕ_{RRE} to address such common rotational Symmetry-Breaking cases.
Initial Weight $\mathbf{W}$
Affine matrix $\mathbf{A}_i^r$ is perturbed by Δ_i
Affine Transformation via $\mathbf{A}_i^r = \mathbf{A}_i^c + \Delta_i$ & Bilinear Interpolation
Relaxed Rotation-Equivariant Filters (R2EFilter)
$\mathbf{F} = \{\mathbf{F}_0, \mathbf{F}_1, \mathbf{F}_2, \mathbf{F}_3\}$
$\mathbf{F}_0$ $\mathbf{F}_1$ $\mathbf{F}_2$ $\mathbf{F}_3$
$\boldsymbol{x}_l$ Input
Convolution operator
$\mathbf{F} * \boldsymbol{x}_l$ Output
Forward
Backward Propagation for End-to-end Update of Δ_i and $\mathbf{W}$

Figure 1: **Left:** The ideal feature of a circle with high-level `SRE` rarely occurs in the real world. Instead, the physical perturbation of `SRE` results in `RRE`. While ENNs can handle `SRE` case, Curie's principle dictates features of higher symmetry cannot be mapped to outputs with lower symmetry, inducing symmetry-breaking situations, and impairing feature learning. `RRE` function ϕ_{RRE} can solve rotational symmetry-breaking situations, which has been proven by Kaba & Ravanbakhsh (2023). **Right:** This work proposes the R2EFilter to build `RRE`, by incorporating learnable perturbation Δ. We show the forward and backward processes of R2EFilter based on relaxed $\mathbf{C}_4$, named $\mathbf{R}_4$.

et al., 2021), ENNs cannot effectively model rotational Symmetry-Breaking, as the requirement for rotation-equivariance of the input data is inherently too restrictive (Kaba & Ravanbakhsh, 2023). Note that symmetry captures the idea that an object is essentially the same after some transformation is applied to it Weyl (1952).

Consider a dataset of images with rotation-equivariance, where each image depicts an object that maintains its structure under rotation. As stated in Curie's principle (Earman, 2004; Chalmers, 1970), the symmetry of a cause is always preserved in its effects, and any asymmetry in the effects must be present in their causes. This implies that an input with higher symmetry cannot be mapped to an output with lower symmetry since the input has no corresponding asymmetry. Conversely, an input with lower symmetry can be mapped to an output with higher symmetry. When an object experiences events such as rotations that exceed the predefined group's scope or the introduction of minor defects on its surface, it implies that the training images and the target object may have different levels of symmetry. In such cases, a strict Equivariant Neural Network (ENN) may encounter difficulties in accurately representing the object, strict adherence to symmetry constraints could prevent it from distinguishing between the object's perturbed and non-perturbed states, which is crucial for specific tasks. Some pioneer works (Locatello et al., 2020; Smidt et al., 2021; Wang et al., 2022a; Kaba & Ravanbakhsh, 2023; Huang et al., 2024; Xie & Smidt, 2024) discussed relaxation of equivariance and claimed that relaxed ENNs can model Symmetry-Breaking in multiple domains. ***However, there is still a significant gap between these existing relaxed ENN works and practical applications of computer vision field, e.g., 2D Object Detection.***

Differing from traditional `SRE` GConv, this work presents a novel Relaxed Rotation-Equivariance (`RRE`) GConv by incorporating a learnable adaptive rotational deviation parameter that is updated end-to-end. Figure 1 details the rotational Symmetry-Breaking problem and our approach. `RRE` enhances the network's ability to recognize objects with relaxed rotational equivariance, effectively tackling the symmetry-breaking problem and capturing distinct features from perturbations, thus promoting performance. The main contributions of this work are as follows:

- We introduce `RRE` into the group convolution operation by simply incorporating learnable perturbations, proposing the Relaxed Rotation-Equivariant Filter (R2EFilter) and the Relaxed Rotation-Equivariant GConv (R2GConv).
- To our knowledge, we are the first to explore rotational Symmetry-Breaking situations within vision tasks. We further propose a Relaxed Rotation-Equivariant Network (R2Net) as a backbone for better capturing `RRE` image features.
- We redesign a Relaxed Rotation-Equivariant Object Detector (R2Det) for 2D object detection. Experimental results show our approaches have achieved better convergence and outstanding performance with lightweight parameters.

2 RELATED WORKS

Advanced 2D Object Detectors. 2D Object Detection (Chen et al., 2023; Zou et al., 2023; Kaur & Singh, 2023) is a fusion of object location and classification tasks, which involves locating objects through bounding boxes and identifying their respective categories. In the field of 2D object detection, several notable methods (Girshick et al., 2014; Liu et al., 2016; Carion et al., 2020; Wang et al., 2021; 2022b) have been developed, and the YOLO framework has stood out for its remarkable balance of speed and accuracy (Redmon et al., 2016; Hussain, 2023; Terven et al., 2023), enabling the rapid and reliable identification of objects in images. Since its inception, the YOLO family has evolved through multiple iterations and variations, such as YOLOv8 (Jocher et al., 2023) YOLOv9 (Wang et al., 2024b), YOLOv10 (Wang et al., 2024a).

Applications of Rotation-Equivariance. The concept of an equivariant network was proposed in Cohen & Welling (2016a), named Group Equivariant Convolution Neural Networks (G-CNN). Rotation-Equivariant convolution or full connect layer (Li et al., 2018; Marcos et al., 2017; Cohen & Welling, 2016a; Finzi et al., 2020) guarantees the rotation-equivariance of extracted features under the group operations by a higher degree of weight sharing. Moreover, Rotation-Equivariance has recently become a strongly desired prior bias in object detection tasks. Han et al. (2021) propose a rotation-equivariant 2D object detector (ReDet) to predict the orientation of aircraft accurately. Most recently, Lee et al. (2024) (FRED) achieves fully Rotation-Equivariant oriented object detection and enables more genuine non-axis-aligned learning. Wang et al. (2023) (DuEqNet) improves 3D object detection performance by constructing a dual-layer object detection network for 3D point clouds with rotation invariance and extracting local-global invariance features. Although Rotation-Equivariance has been considered, there is a naive assumption of uniform strict symmetry across all features, neglecting scenarios that require a relaxation of equivariant constraints.

Symmetry-Breaking. Physical laws are governed by numerous symmetries and real-world data, such as complex datasets and graphs. However, it often deviates from strict mathematical symmetry due to noisy or incomplete data or inherent Symmetry-Breaking features in the underlying system. Several works aim to break the symmetry. Wang et al. (2022a) investigates approximately equivariant networks by incorporating relaxed weight sharing in group convolutions and weight-tying in steerable CNNs, respectively, thereby achieving a bias toward not strictly preserving symmetry. Kaba & Ravanbakhsh (2023) proposes a novel theoretical guidance for constructing relaxed equivariant multilayer perceptrons, going beyond the straightforward approach of adding noise to inputs and using an ENN (Locatello et al., 2020). Huang et al. (2024) tackles graph symmetry in real-world data by leveraging graph coarsening to establish approximate symmetries and propose a bias-variance tradeoff formula based on symmetry group selection. Xie & Smidt (2024) introduces Symmetry-Breaking parameters sampled as model inputs from a set determined solely by input and output symmetries. They further observe that breaking more symmetry than needed is beneficial.

In a nutshell, real-world data rarely conforms to strict symmetry. Diverse objects inherently possess levels of relaxed symmetry, regardless of modality, e.g., 2D images or 3D vision data (Kaba & Ravanbakhsh, 2023). Consequently, existing methods fail to tackle Symmetry-Breaking issues, affecting downstream task performance. To our knowledge, we are the first to address these limitations in the 2D object detection field by adopting the rotational Symmetry-Breaking and `RRE` perspective.

3 PROPOSED METHOD

3.1 PRELIMINARY

Definition 1 (*Strict Equivariance*). *A learning function* $\phi_{strict} : X \rightarrow Y$ *that sends elements from input space* X *to output space* Y *satisfies Strict Equivariance to a group* G *if* $\forall g, \mathbf{x} \in G \times X$ *there exists* $\rho_X : G \rightarrow \mathrm{GL}(X)$ *and* $\rho_Y : G \rightarrow \mathrm{GL}(Y)$ *actions of* G *such that*

$$\phi_{strict}\left(\rho_X(g) \cdot \mathbf{x}\right) = \rho_Y(g) \cdot \phi_{strict}(\mathbf{x}), \tag{1}$$

where $\mathrm{GL}(\cdot)$ *is a general linear group over the space.*

Definition 2 (*Relaxed Equivariance*). (Kaba & Ravanbakhsh, 2023) *A learning function* $\phi_{relaxed} : X \rightarrow Y$ *that sends elements from input space* X *to output space* Y *satisfies Relaxed Equivariance to a group* G *if* $\forall g_1, \mathbf{x} \in G \times X$ *there exists* $g_2 \in g_1 G_{\mathbf{x}}$, $\rho_X : G \rightarrow \mathrm{GL}(X)$ *and* $\rho_Y : G \rightarrow \mathrm{GL}(Y)$

actions of G such that

$$\phi_{relaxed}(\rho_X(g_1)\cdot\mathbf{x}) = \rho_Y(g_2)\cdot\phi_{relaxed}(\mathbf{x}), \tag{2}$$

Definition 3 (*Approximate Equivariance*). (Wang et al., 2022a) *A learning function $\phi_{approx}: X \rightarrow Y$ that sends elements from input space X to output space Y satisfies Relaxed Equivariance to a group G if $\forall g, \mathbf{x} \in G \times X$ there exists $\rho_X : G \rightarrow \mathrm{GL}(X)$ and $\rho_Y : G \rightarrow \mathrm{GL}(Y)$ actions of G such that*

$$\|\phi_{approx}(\rho_X(g)\cdot\mathbf{x}) - \rho_Y(g)\cdot\phi_{approx}(\mathbf{x})\| \le \epsilon, \tag{3}$$

where a small ϵ indicates strong symmetry and a relatively larger (not very large) ϵ exhibits greater relaxation. Especially, ϕ_{approx} is equivalent to ϕ_{strict} and also satisfies Equation 1 when $\epsilon = 0$.

Approximate equivariance can be regarded as a case of relaxed equivariance, and they are solving the same problem, i.e., Symmetry-Breaking. The definition of relaxed equivariance is broader and does not provide a quantifiable degree of relaxation. However, approximate equivariance considers symmetry to be broken to a certain degree, with ϵ as the upper bound, making it more applicable and encountered in real-world scenarios. Therefore, in this work, we further assume that the symmetry-breaking encountered in visual image data under rotations can be better addressed by constructing a relaxed equivariant function that also satisfies the conditions of approximate equivariance, i.e., we have the learning function ϕ_{approx} satisfies that if $\forall g, \mathbf{x} \in G \times X$ there exists $g_1 \in gG_{\mathbf{x}}$, $g_2 \in gG_{\mathbf{x}}$, $\rho_X : G \rightarrow \mathrm{GL}(X)$ and $\rho_Y : G \rightarrow \mathrm{GL}(Y)$ actions of G such that

$$\begin{aligned} &\|\phi_{approx}(\rho_X(g)\cdot\mathbf{x}) - \rho_Y(g)\cdot\phi_{approx}(\mathbf{x})\| \le \epsilon, \\ s.t.\ \phi_{approx} = \phi_{relaxed},\ &\phi_{relaxed}(\rho_X(g_1)\cdot\mathbf{x}) = \rho_Y(g_2)\cdot\phi_{relaxed}(\mathbf{x}). \end{aligned} \tag{4}$$

This allows us to introduce and implement the relaxed rotation-equivariant filter while retaining the benefits of both relaxed and approximate equivariance. We provide more analysis in Appendix A.11.

Strict Equivariant Neural Networks. Learning equivariant features is an optimization process for a series of ϕ_{strict} function sets in the model. However, the challenge of strict equivariant networks lies in designing trainable layers, such as equivariant convolutions. Usually, there are two strategies for designing equivariant convolutions: weight sharing and weight typing, which are G-CNN and G-steerable CNN (Cohen & Welling, 2016b), respectively.

Relaxed Equivariant Neural Networks. The existing equivariant networks assume that the data is completely symmetric. This network approximates a strict invariant or equivariant function under given group actions. For example, in G-CNN, the shared convolution filters achieve equivariant images at 0, 90, 180, and 270 degrees under the strict constraint of $\mathbf{C}_4$. However, real-world data is rarely symmetric. This seriously hinders the potential application of equivariant networks. To solve this problem, in Elsayed et al. (2020) and Wang et al. (2022a), relaxing weight constraints can significantly improve the performance and generalization ability of the model. This work relaxes strict group constraints for a relaxed equivariant neural network.

3.2 RELAXED ROTATION-EQUIVARIANT FILTER (R2EFILTER)

In the following, we denote all $i \in \{0, 1, \cdots, n-1\}$ for convenient presentation. We first introduce Relaxed Rotation-Equivariant Filter (R2EFilter) denoted by F, serves as the crucial component of R2GConv. To relax strict group constraints, R2EFilter embeds a learnable parameter Δ to perturb the group operation based on the n-order cyclic rotation group $\mathbf{C}_n = \{\mathbf{c}^i \mid i = 0, 1, \cdots, n-1\}$, a discrete and finite subgroup of SO(2), which an infinite group that contains a set of all two-dimensional rotation angles. The powers of $\mathbf{c}^i$ indicates performing rotation operation on the input $\mathbf{x}$ by $\frac{2\pi i}{n}$ degrees, i times. The affine matrix $\mathsf{A}_i^{\mathbf{c}}$ on $\mathbf{C}_n$ can be defined as follows:

$$\mathsf{A}_i^{\mathbf{c}} = \begin{bmatrix} \cos(2\pi i/n) & -\sin(2\pi i/n) \\ \sin(2\pi i/n) & \cos(2\pi i/n) \end{bmatrix}. \tag{5}$$

Further, let the learnable perturbation factor $\Delta \in \mathbb{R}^{n\times 2\times 2} \leftarrow \mathcal{U}(-b, b)$, where $\mathcal{U}$ denotes Uniform distribution with boundary value b. Our original intention is to provide an appropriate level of initial perturbation to fit Δ to a suitable value. In Section 4, we conduct several experiments with different b from 0 to 0.8, where the experimental results show that a small value of b enhances the model's performance, whereas a large value of b detrimentally affects the model's performance.

Then, we can define $\Delta = \{\Delta_i\}, \Delta_i = [\Delta_{i1}, \Delta_{i2}, \Delta_{i3}, \Delta_{i4}]$ and a Relaxed Rotation-Equivariant group $\mathbf{R}_n = \{\mathbf{r}^i\}$ based on $\mathbf{C}_n$ and a transformation function $\mathcal{T} : \mathbf{C}_n \rightarrow \mathbf{R}_n$. We consider $\mathcal{T}$ as an addition, i.e., adding the learnable perturbation factor Δ_i to the affine matrix $\mathbf{A}_i^{\mathbf{c}}$. Thus, the perturbed affine matrix $\mathbf{A}_i^{\mathbf{r}}$ on $\mathbf{R}_n$ is defined as $\mathbf{A}_i^{\mathbf{r}} = \mathcal{T}(\mathbf{A}_i^{\mathbf{c}}, \Delta_i) = \mathbf{A}_i^{\mathbf{c}} + \Delta_i$, where other operations are also available for $\mathcal{T}$, such as multiplication, and linear transformation, but are not limited to.

Here, we explain the affine transformation from the perspective of coordinate changes. Specifically, given $\mathbf{W}$ as a Kaiming-Initialization (He et al., 2015) 2D convolution weight, and $\mathbf{F}$ denotes the transformed filter on $\mathbf{R}_n$. Consider this example, let a function $\texttt{CoorSet}(\cdot)$ denote a set of 2D coordinates of the elements in $\cdot$, where the coordinate system is at the center of $\cdot$. For all coordinates $[u\ v] \in \texttt{CoorSet}(\mathbf{W})$, we have two affine transformations: $\mathbf{c}^i([u\ v]) = \mathbf{A}_i^{\mathbf{c}} \cdot [u\ v]^\top$ and $\mathbf{r}^i([u\ v]) = \mathbf{A}_i^{\mathbf{r}} \cdot [u\ v]^\top$ on $\mathbf{C}_n$ and $\mathbf{R}_n$, respectively. The transformed coordinates $[\tilde{u}_i\ \tilde{v}_i]$ for $\mathbf{F}_i$ are as follows:

$$\mathbf{r}^i([u\ v]) = \left(\begin{bmatrix} \cos(2\pi i/n) + \Delta_{i1} & -\sin(2\pi i/n) + \Delta_{i2} \\ \sin(2\pi i/n) + \Delta_{i3} & \cos(2\pi i/n) + \Delta_{i4} \end{bmatrix} \begin{bmatrix} u \\ v \end{bmatrix} \right), \quad [\tilde{u}_i\ \tilde{v}_i] = \left\lfloor \left(\mathbf{r}^i([u\ v]) \right)^\top \right\rfloor, \tag{6}$$

where $\lfloor \cdot \rfloor$ denotes the round down operation for $\cdot$. Further, if $[\tilde{u}_i\ \tilde{v}_i] \in \texttt{CoorSet}(\mathbf{F}_i)$, we set $\mathbf{F}_i[\cdots, \tilde{u}, \tilde{v}] := \mathbf{W}[\cdots, u, v]$. For coordinates $[\dot{u}_i\ \dot{v}_i]$ in $\mathbf{F}_i$ that remain unassigned after mapping from $\mathbf{W}$, we employ the ***Bilinear Interpolation*** method to fill $\mathbf{F}_i[\cdots, \dot{u}_i, \dot{v}_i]$. Then, we have the complete R2EFilter: $\mathbf{F} = \{\mathbf{F}_i\}$. The construction process of $\mathbf{F}$ is detailed in Algorithm 1. In the rest of this work, this process is abstracted by the mapping function Ψ, i.e., $\mathbf{F} = \Psi(\mathbf{W})$.

Algorithm 1 Build R2EFilter based on $\mathbf{C}_n$.

```
Input: The group order $n$ of $\mathbf{C}_n$; The boundary value $b$ of Uniform distribution $\mathcal{U}(-b, b)$; The Kaiming-Initialization $\mathbf{W}$.
Output: The R2EFilter based on $\mathbf{C}_n$: $\mathbf{F}$.
Initialize $\mathbf{F} \leftarrow \emptyset$                                   ▷ Empty $\mathbf{F}$ to store compelete R2EFilter
Initialize $\Delta \in \mathbb{R}^{n \times 2 \times 2} \leftarrow \mathcal{U}(-b, b)$    ▷ Learnable perturbation factor with Uniform distribution
$s \leftarrow$ Get_Tensor_Shape ($\mathbf{W}$)                             ▷ Get the tensor shape
$c \leftarrow$ Get_Output_Channels ($\mathbf{W}$)                          ▷ Get the output channels
for $i = 0$ to $(n-1)$ do                                              ▷ Loop the group order $n$
    $\mathbf{A}_i \leftarrow \begin{bmatrix} \cos(2\pi i/n) + \Delta_{i1} & -\sin(2\pi i/n) + \Delta_{i2} & 0 \\ \sin(2\pi i/n) + \Delta_{i3} & \cos(2\pi i/n) + \Delta_{i4} & 0 \end{bmatrix}$    ▷ Get the perturbed affine matrix
    $\mathbf{A}_i^c \leftarrow$ Repeat_Tensor ($\mathbf{A}_i, c$)                  ▷ Repeat $\mathbf{A}_i$ for $c$ times
    $\mathbf{G}_i \leftarrow$ Affine_Grid ($\mathbf{A}_i^c, s$)                   ▷ Generate affine grid $\mathbf{G}_i$
    $\mathbf{F}_i \leftarrow$ Grid_Sample ($\mathbf{W}, \mathbf{G}_i$)            ▷ Sampling on $\mathbf{G}_i$ to get the $i$-order filter $\mathbf{F}_i$
    Update $\mathbf{F} \leftarrow \mathbf{F} \cup \mathbf{F}_i$
end for
return $\mathbf{F}$
```

3.3 RELAXED ROTATION-EQUIVARIANT GCONV (R2GCONV)

So far, by relaxing strict constraints of group operations on $\mathbf{C}_n$ through learnable perturbation factor Δ, we have defined the Relaxed Rotation-Equivariant group $\mathbf{R}_n$ and achieved R2EFilter. Based on it, we introduce a Relaxed Rotation-Equivariant GConv (R2GConv), encompassing three variants: Lifting R2GConv, Point-wise R2GConv, and Depth-wise R2GConv.

Specifically, since the input image and traditional convolution filters are on the plane, Lifting R2GConv is designed as an equivariant transformation to replace conventional translation operations. It is applied in the first layer to convert the input data into feature maps on a specific group (e.g., $\mathbf{R}_n$ in this work), enabling more complex and structured feature extraction. For subsequent layers, filters of Point-wise R2GConv and Depth-wise R2GConv are defined on $\mathbf{R}_n$, facilitating the equivariant transformation and processing of these feature maps. The point-wise and depth-wise strategies in R2GConv avoid the inevitably substantial parameters and computational overhead associated with GConv operations. Meanwhile, the reduced number of parameters also diminishes the computational complexity and required time to build their filters with R2EFilter. Based on this reason, we combine Point-wise R2GConv and Depthwise R2GConv to propose an Efficient R2GConv.

For convenience, in the following, let n_l, c_l, c_{l+1}, k_l, h_l, and w_l denote the group order, the number of input channels, the number of output channels, convolution kernel size, input height, and input width in the l-layer, respectively.

- **R2GConv.** Consider the input feature map $\boldsymbol{x}_l \in \mathbb{R}^{c_l n_l \times h_l \times w_l}$ and an initial convolution weight $\mathbf{W}_l \in \mathbb{R}^{c_{l+1} \times c_l n_l \times k_l \times k_l}$, where $l > 1$. Traditional convolution computes the output feature map on a plane by performing an inner product between the input feature map and the convolution filter, with the filter shifted by a defined step. According to Section 3.2, we have R2EFilter $\mathbf{F}_l = \Psi(\mathbf{W}_l) \in \mathbb{R}^{c_{l+1}n_{l+1} \times c_l n_l \times k_l \times k_l}$, where $n_{l+1} = n_l = n$. Thus R2GConv transforms the input feature map $\boldsymbol{x}_l$ to the output feature map $\boldsymbol{x}_{l+1} \in \mathbb{R}^{c_{l+1}n_{l+1} \times h_{l+1} \times w_{l+1}}$ as follows:

$$\underbrace{\boldsymbol{x}_{l+1}[d,:,:]}_{h_{l+1} \times w_{l+1}} = \sum_{c=0}^{c_l n_l - 1} \underbrace{\mathbf{F}_l[d,c,:,:]}_{k_l \times k_l} * \underbrace{\boldsymbol{x}_l[c,:,:]}_{h_l \times w_l}, \quad \forall d \in \{0, \cdots, c_{l+1}n_{l+1} - 1\}, \tag{7}$$

where $*$ denotes vanilla convolution operation. We also prove that our R2GConv is the `RRE` block that conforms to Eq. (2), as shown in Appendix A.10.

- **Lifting R2GConv.** Considering the special case where R2GConv is employed in the first layer, i.e., $l = 1$, to lift the input feature map $\boldsymbol{x}_1 \in \mathbb{R}^{c_1 \times h_1 \times w_1}$ onto $\mathbf{R}_n$, called Lifting R2GConv. Thus, we have its R2EFilter $\mathbf{F}_1 = \Psi(\mathbf{W}_1) \in \mathbb{R}^{c_2 n_2 \times c_1 n_1 \times k_1 \times k_1}$, where $n_1 = 1, n_2 = n$. Further, the output feature map $\boldsymbol{x}_2 \in \mathbb{R}^{c_2 n_2 \times h_2 \times w_2}$ is obtained as follows:

$$\underbrace{\boldsymbol{x}_2[d,:,:]}_{h_2 \times w_2} = \sum_{c=0}^{c_1 - 1} \underbrace{\mathbf{F}_1[d,c,:,:]}_{k_1 \times k_1} * \underbrace{\boldsymbol{x}_1[c,:,:]}_{h_1 \times w_1}, \quad \forall d \in \{0, \cdots, c_2 n_2 - 1\}. \tag{8}$$

- **Point-wise R2GConv.** In the l-layer with $l > 1$, given the input feature map $\boldsymbol{x}_l \in \mathbb{R}^{c_l n_l \times h_l \times w_l}$ and an initial convolution weight $\mathbf{W}_l^{\mathrm{p}} \in \mathbb{R}^{c_{l+1} \times c_l n_l \times 1 \times 1}$, we have $\mathbf{F}_l^{\mathrm{p}} = \Psi(\mathbf{W}_l^{\mathrm{p}}) \in \mathbb{R}^{c_{l+1}n_{l+1} \times c_l n_l \times 1 \times 1}$, where $n_l = n_{l+1} = n$. Since the size of filter $\mathbf{F}_l^{\mathrm{p}}$ is always 1×1, the Point-wise R2GConv is considered the standard point-wise convolution operation, which is defined as follows:

$$\underbrace{\boldsymbol{x}_{l+1}[d,:,:]}_{h_{l+1} \times w_{l+1}} = \sum_{c=0}^{c_l n - 1} \underbrace{\mathbf{F}_l^{\mathrm{p}}[d,c,:,:]}_{1 \times 1} * \underbrace{\boldsymbol{x}_l[c,:,:]}_{h_l \times w_l}, \quad \forall d \in \{0, \cdots, c_{l+1}n_{l+1} - 1\}. \tag{9}$$

- **Depth-wise R2GConv.** Given the input feature map $\boldsymbol{x}_l \in \mathbb{R}^{c_l n_l \times h_l \times w_l}$ and an initial convolution weight $\mathbf{W}_l^{\mathrm{d}} \in \mathbb{R}^{c_{l+1} \times 1 \times k_l \times k_l}$ in the l-layer with $l > 1$, we have $\mathbf{F}_l^{\mathrm{d}} = \Psi(\mathbf{W}_l^{\mathrm{d}}) \in \mathbb{R}^{c_{l+1}n_{l+1} \times 1 \times k_l \times k_l}$, where $n_l = n_{l+1} = n$. Consequently, Depth-wise R2GConv is defined as follows:

$$\underbrace{\boldsymbol{x}_{l+1}[d,:,:]}_{h_{l+1} \times w_{l+1}} = \underbrace{\mathbf{F}_l^{\mathrm{d}}[d,:,:,:]}_{1 \times k_l \times k_l} *_{\mathrm{D}} \underbrace{\boldsymbol{x}_l[:,:,:]}_{c_l n_l \times h_l \times w_l}, \quad \forall d \in \{0, \cdots, c_{l+1}n_{l+1} - 1\}, \tag{10}$$

where $*_{\mathrm{D}}$ denotes the depth-wise operation with the convolution group number $c_{l+1}n_{l+1}$, which needs to meet $c_l / c_{l+1} \in \mathbb{Z}^+$ for the correct division of convolution group number.

- **Efficient R2GConv.** Here, we propose an Efficient R2GConv as $\boldsymbol{x}_{l+1} = \mathbf{F}_l^{\mathrm{d}} *_{\mathrm{D}} (\mathbf{F}_l^{\mathrm{p}} * \boldsymbol{x}_l)$ in the l-layer, where $n_l = n_{l+1} = n$. Note that the point-wise operation is used for channel connection, while the depth-wise operation reduces the high parameters and computation. With these operations, the model's performance can be effectively maintained while achieving parameter reduction.

3.4 THE RELAXED ROTATION-EQUIVARIANT NETWORK (R2NET)

Based on R2GConv, we further propose a Relaxed Rotation-Equivariant Network (R2Net), as shown in Figure 2. R2Net comprises a Lifting R2GConv and the standard four-stage processing used for most backbone networks. In the first layer, we typically project the input tensor to our defined group $\mathbf{R}_n$ while performing $2\times$ downsampling by a Lifting R2GConv with stride 2. Then, we input the projected tensor into the four-stage processing. Each stage incorporates an Efficient R2GConv with stride 2 for $2\times$ downsampling, followed by an R2Net Block for feature extraction. In the last stage, we maintain the output channels unchanged compared to the input channels, which mainly reduces the number of parameters. Regarding R2Net Block, we borrow the idea of dividing channels in Res2Net (Gao et al., 2019) to reduce the number of parameters and FLOPs. In the R2Net Block, we initially apply a Point-wise R2GConv for the channel change and then split the channel. Subsequently, for each channel after the first one, we aggregate it with the previous channel before feeding it into its corresponding Bottleneck, which is composed of two stacked Efficient R2GConv modules with a residual connection (He et al., 2016) structure to improve the convergence ability.

Here, we provide our R2Net with three sizes: R2Net-N, R2Net-S, and R2Net-M, with the suffixes "-N", "-S" and "-M" indicating the Nano size (as introduced above), Small size, and Medium size, respectively. Detailed parameter settings of R2Net can be found in Appendix A.1.

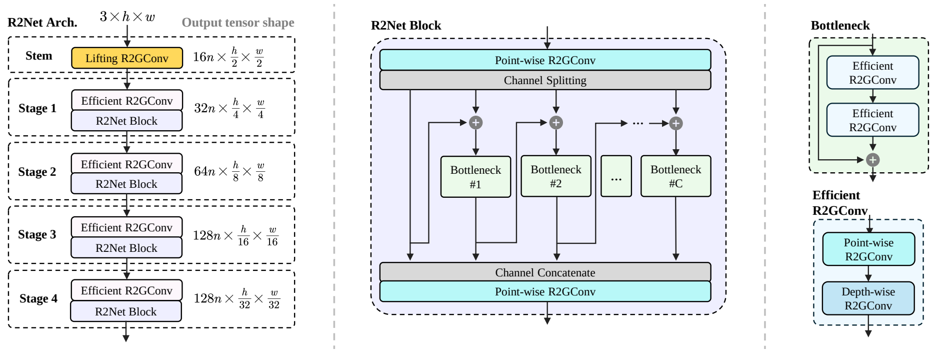

Figure 2: The architecture of R2Net-N as the backbone for feature extraction, where #C denotes the number of Bottlenecks in R2Net Blocks based on the channel sizes and varies with the different sizes of R2Net (i.e., R2Det-N / S / M). Note that all R2GConv including three variants have normalization (BatchNorm) and activation (SiLU) functions, which we do not show in the figure.

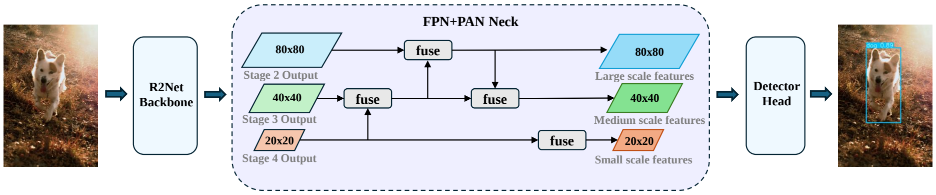

Figure 3: The architecture of R2Det for 2D object detection with a FPN+PAN neck. Here, we only show a simple architectural diagram. For detailed architecture, please refer to Appendix A.2.

3.5 THE REDESIGNED RELAXED ROTATION-EQUIVARIANT OBJECT DETECTOR (R2DET)

Based on the backbone R2Net, we propose a novel Relaxed Rotation-Equivariant Object Detector (R2Det). R2Det employs the Feature Pyramid Network (FPN) + Path Aggregation Network (PAN) neck architecture, as shown in Figure 3. Specifically, R2Net mainly extracts multi-scale features in R2Det. The neck part in R2Det further aggregates information from multiple paths, allowing for enhanced communication between different levels of the feature pyramid.

Following three sizes of R2Net, we also provide our R2Det with three sizes: R2Det-N, R2Det-S, and R2Det-M. More detailed parameter settings of R2Det can be found in Appendix A.1.

4 EXPERIMENTS

4.1 2D OBJECT DETECTION ON THE PASCAL VOC AND MS COCO DATASETS

To investigate the effectiveness of our method, we conduct extensive experiments on the MSCOCO 2017 (COCO) and PASCAL VOC07+12 (VOC) datasets. We set $b = 0.1$, and the `RRE` (or `SRE`) is constructed on $\mathbf{C}_4$ in all experiments if not specified.

Effect of b in Uniform distribution $\mathcal{U}(-b, b)$ on `RRE`. We explore the impact of the boundary value b of uniform distribution $\mathcal{U}(-b, b)$ for the perturbation on model performance, where a larger value of b indicates a greater initial perturbation Δ and has a higher level of `RRE` in R2GConv. Table 1 demonstrate that R2Det-N with $b = 0.1$ achieve the best results in both $\mathbf{AP}_{50:95}$ and $\mathbf{AP}_{50}$, outperforming those with initializations of 0 or too large values. Figure 4a further demonstrates the training curves of our R2Det-N ($\mathbf{C}_4$) with varying b on VOC dataset. Since the Δ in R2GConv can be readjusted by end-to-end learning strategy, we suggest that a small initial perturbation can better align Δ to the rotational Symmetry-Breaking property of natural image datasets. Additionally, we provide specific Δ values in four Efficient R2GConv, as shown in Appendix A.4. Note that R2Det (`RRE`) with $b = 0$ is not equivalent to R2Det (`SRE`), as Δ with an initial value of 0 still achieves end-to-end updates by gradient descent.

Covergence analysis. We analyze the convergence of our R2Det and YOLOv8 models during the training process on the VOC training dataset, as shown in Figure 4b. Both R2Det-S / M converge

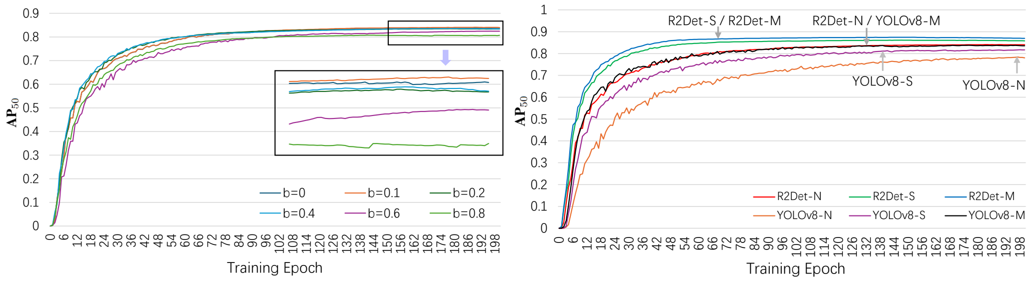

(a) $\mathbf{AP}_{50}$ of R2Det with different b (b) $\mathbf{AP}_{50}$ comparison of R2Det and YOLOv8.

Figure 4: $\mathbf{AP}_{50}$ curves on VOC test dataset. All models train for 200 epochs with the same settings.

in about 66 epochs, much earlier than YOLOv8-S / M, which converge in about 138 epochs and 132 epochs, respectively. Furthermore, YOLOv8-N converges in about 198 epochs, while R2Det-N converges in about 132 epochs, the same as YOLOv8-M. It is worth noting that the convergence curve of R2Det is smoother than YOLOv8, demonstrating a better convergence process of R2Det. Overall, our R2Det models of all three variants (N / S / M) exhibit not only outstanding performance in $\mathbf{AP}_{50}$ but also a more stable training process with faster convergence speed compared to YOLOv8 models. The faster convergence could be related to the fact that our R2GConv can extract rich and relaxed equivariant features, enabling earlier learning of these potential features.

Table 1: Results of R2Det-N ($\mathbf{C}_4$) with different boundary value b on VOC test dataset.

b	$\mathbf{AP}_{50}(\%)$	$\mathbf{AP}_{50:95}(\%)$
0	83.8	64.4
0.1	**84.1**	**65.1**
0.2	83.5	64.3
0.4	83.6	64.4
0.6	82.4	62.6
0.8	80.7	59.7

Table 2: Alabtion experiments of R2Det-N with `SRE` and `RRE` (ours) on VOC test dataset.

Group	Equiv.	$\mathbf{AP}_{50:95}(\%)$	$\mathbf{AP}_{50}(\%)$	Params.	FLOPs
$\mathbf{C}_2$	`SRE`	58.4	78.1	1.8M	3.2G
	`RRE`	**59.0** (+0.6)	**79.4** (+1.3)	1.8M + 0.256K	3.2G
$\mathbf{C}_4$	`SRE`	64.2	82.9	2.6M	3.3G
	`RRE`	**65.1** (+0.9)	**84.1** (+1.2)	2.6M + 0.512K	3.3G
$\mathbf{C}_8$	`SRE`	65.5	84.2	4.4M	3.7G
	`RRE`	**67.0** (+1.5)	**85.4** (+1.2)	4.4M + 1.024K	3.7G

Table 3: Alabtion experiments of R2Det-N with `SRE` and `RRE` (ours) on COCO validation dataset.

Group	Equiv.	$\mathbf{AP}_{50:95}(\%)$	$\mathbf{AP}_{75}(\%)$	$\mathbf{AP}_{50}(\%)$	$\mathbf{AP}_{S}(\%)$	$\mathbf{AP}_{M}(\%)$	$\mathbf{AP}_{L}(\%)$	Params.	FLOPs
$\mathbf{C}_2$	`SRE`	36.2	39.5	51.0	18.2	39.8	50.7	1.9M	3.8G
	`RRE`	**36.6** (+0.4)	**39.8** (+0.3)	**51.5** (+0.5)	**19.4** (+1.2)	**39.9** (+0.1)	**51.5** (+0.8)	1.9M + 0.256K	3.8G
$\mathbf{C}_4$	`SRE`	43.2	47.4	58.7	22.6	48.1	58.3	2.8M	4.0G
	`RRE`	**43.7** (+0.5)	**47.8** (+0.4)	**59.5** (+0.8)	**24.2** (+1.6)	**48.2** (+0.1)	**59.3** (+1.0)	2.8M + 0.512K	4.0G
$\mathbf{C}_8$	`SRE`	46.8	62.2	51.0	26.0	52.7	62.1	4.5M	4.3G
	`RRE`	**47.5** (+0.7)	**63.7** (+0.5)	**52.1** (+1.1)	**27.9** (+1.9)	**52.9** (+0.2)	**63.4** (+1.3)	4.5M + 1.024K	4.3G

- Note that "Equiv." denotes the type of rotation-equivariant filter used in R2Det, as `SRE` indicates regular Strict Rotation-Equivariant Filter, whereas `RRE` means our proposed Relaxed Rotation-Equivariant Filter (R2EFilter).

Ablation experiments evaluating `RRE` vs. `SRE` on COCO and VOC. We first conduct ablation experiments on COCO and VOC datasets to discuss the effectiveness of `RRE`, comparing it with `SRE`, based on three groups, including $\mathbf{C}_2$, $\mathbf{C}_4$, and $\mathbf{C}_8$. As shown in Table 2 and Table 3, R2Det-N (`RRE`) outperforms R2Det-N (`SRE`) in all average precision (**AP**) metrics. These results demonstrate that `RRE` can effectively overcome the limitations of `SRE` mentioned above. Meanwhile, compared to R2Det-N (`SRE`), our approach results in a negligible increase in parameters quantity (**Params.**) and floating point operations (**FLOPs**) compared to R2Det-N (`SRE`), improving model performance with **almost negligible** parameter increase (i.e., 256 / 512 / 1024) on $\mathbf{C}_2$ / $\mathbf{C}_4$ / $\mathbf{C}_8$.

Inability of naive convolutions with learnable noise to construct `RRE`. We conduct experiments that incorporate learnable noise into the traditional convolution filters of YOLOv8 to evaluate its impact on convolution filters. As shown in Table 4, simply adding noise to the filters of the original convolution leads to degraded model performance. This suggests that for operators like the original convolution, which lack inherent rotation-equivariance properties, simply adding noise does not confer achieving `RRE` to handle data exhibiting rotational Symmetry-Breaking.

Plug-and-play and generalization ability. We show that by simply replacing and plugging, our proposed modules mentioned in Section 3.3 can effectively transfer the `RRE` property to other archi-

Table 4: Alabtion experiments of naive convolution filter w/ (w/o) learnable noise of YOLOv8-N on VOC test dataset.

Type	**AP**$_{50}$(%)	**AP**$_{50:95}$(%)
w/o noise	78.6	57.5
w/ noise	73.1 (-5.5)	51.4 (-6.1)

Table 5: Alabtion experiments of YOLOv8-N architecture on $\mathbf{C}_4$ on VOC test dataset.

Equiv.	**AP**$_{50:95}$(%)	**AP**$_{50}$(%)	**Params.**
`NRE`	57.5	78.6	3.3M
`SRE`	62.8	82.7	3.2M
`RRE`	**64.2** (+1.4)	**83.6** (+0.9)	3.2M

tectures, such as YOLOv8 architecture. Specifically, we replace the first layer Conv of YOLOv8-N with Lifting R2GConv and replace all other intermediate layer Convs with our Efficient R2GConv. From Table 5, YOLOv8-N (`RRE`) also surpass YOLOv8-N (`SRE`) and YOLOv8-N (`NRE`) in both **AP**$_{50:95}$ and **AP**$_{50}$. Note that YOLOv8-N (`NRE`) means the standard YOLOv8-N model. This experiment demonstrates that our R2GConv is plug-and-play and still effective in other architectures, demonstrating its generalization ability.

Table 6: Comparison with the latest state-of-the-art object detectors on COCO validation dataset.

Method	**AP**$_{50:95}$(%)	**AP**$_{50}$(%)	**AP**$_{75}$(%)	**AP**$_{S}$(%)	**AP**$_{M}$(%)	**AP**$_{L}$(%)	**Params.**	**FLOPs**
YOLOv8-N	37.3	52.6	40.5	18.6	41.0	53.5	3.2M	8.7G
YOLOv8-S	44.9	61.8	48.7	26.0	49.9	61.1	11.2M	28.6G
YOLOv8-M	50.2	67.2	54.7	32.3	55.9	66.5	25.9M	78.9G
YOLOv8-L	52.9	69.8	57.5	35.3	58.3	69.8	43.7M	165.2G
YOLOv9-T	38.3	53.1	41.3	-	-	-	2.0M	7.7G
YOLOv9-S	46.8	63.4	50.7	26.6	56.0	64.5	7.1M	26.4G
YOLOv9-M	51.4	68.1	56.1	33.6	57.0	68.0	20.0M	76.3G
YOLOv9-C	53.0	70.2	57.8	36.2	58.5	69.3	25.3M	102.1G
YOLOv10-N	38.5	53.8	41.7	18.9	42.4	54.6	2.3M	6.7G
YOLOv10-S	46.3	63.0	50.4	26.9	51.1	63.7	7.2M	21.6G
YOLOv10-M	51.1	68.1	55.8	33.8	56.5	67.0	15.4M	59.1G
YOLOv10-B	52.5	69.6	57.2	35.1	57.8	68.4	19.1M	92.0G
YOLOv10-L	53.2	70.1	58.0	35.7	58.4	69.4	24.4M	120.3G
R2Det-N (C_4)	43.7	59.5	47.8	24.2	48.2	59.3	2.8M	4.0G
R2Det-S (C_4)	50.0	66.5	54.6	30.5	55.7	66.2	9.6M	9.0G
R2Det-M (C_4)	53.1	70.3	57.9	36.4	58.7	69.6	22.6M	17.3G

Average precision comparison. As detailed in Table 6, we compare our proposed R2Det with advanced YOLO-serie detectors on COCO validation dataset. Since both YOLOv8 and R2Det offer N / S / M variants, each of which is compared individually. Despite having 12.5% / 14.3% / 12.7% fewer parameters, R2Det achieves significant improvements of 17.2% / 11.4% / 5.8% in **AP**$_{50:95}$, compared to YOLOv8, respectively. Then, we compare R2Det to the latest advanced models. Also on N / S / M three variants, although these models have fewer parameters than R2Det, we achieve **AP**$_{50:95}$ improvements by 14.1% / 6.8% / 3.3% compared to YOLOv9, and 13.5% / 8% / 3.9% compared to YOLOv10. Moreover, while R2Det-M has approximately half the number of parameters of YOLOv8-L and lower FLOPs than YOLOv9-C and YOLOv10-L, it consistently outperforms YOLOv8-L, YOLOv9-C, and YOLOv10-B in **AP** across all IoU thresholds and for objects of different sizes. In addition, R2Det-M achieves approximate results compared to YOLOv10-L, but its parameters are fewer. We further conduct experiments on VOC dataset as shown in Table 7. In each variant comparison, R2Det exceeds YOLOv8 in **AP**$_{50}$ by 13.1% / 7.6% / 4.6%, for the N, S, and M variants, respectively. R2Det-M achieves state-of-the-art performance in **AP**$_{50}$ on VOC with only one-third parameters of YOLOv8-L. Experimental results above show that our R2Det has achieved excellent performance in **AP** with fewer parameters and much lower FLOPs than existing state-of-the-art object detectors. Please refer to Appendix A.12 for more results and comparisons.

Table 7: Comparison with advanced YOLOv8 models on VOC test dataset.

Method	**AP**$_{50}$(%)	**Params.**	**FLOPs**
YOLOv8-N	78.6	3.0M	8.1G
YOLOv8-S	81.6	11.1M	28.5G
YOLOv8-M	83.7	25.9M	78.7G
YOLOv8-L	86.4	43.6M	164.9G
YOLOv8-X	86.9	68.1M	257.5G
R2Det-N (C_4)	84.1	2.6M	3.3G
R2Det-S (C_4)	86.0	9.6M	8.9G
R2Det-M (C_4)	**87.3**	22.6M	17.2G

Table 8: Comparison with other models in Top-1 Accuracy (%) on CIFAR-10 / 100 datasets.

Method	**C-10**(%)	**C-100**(%)	**Params.**
WideResNet	95.8	79.5	36.5M
ResNeXt-29	96.4	82.7	68.1M
DenseNet-BC	96.5	**82.8**	25.6M
R2Net-N (C_4)	95.8	80.6	0.9M
R2Net-S (C_4)	96.6	82.2	2.8M
R2Net-M (C_4)	**97.3**	82.7	6.0M

4.2 ADDITIONAL EXPERIMENTS

Image Classification. Classification evaluation assesses the discriminative quality of features. We construct the backbone R2Net incorporating v8Classify Head for image classification tasks, as depicted in Figure 3. Table 8 shows the top-1 accuracy of R2Net in three sizes (-N / S / M) on CIFAR-10 / 100 datasets. R2Net and all outstanding baselines trained from scratch. In CIFAR-10, R2Net-M achieves superior accuracy with significantly fewer parameters than DenseNet-BC, WideResNet, and ResNeXt. In CIFAR-100, R2Net-N has only 2.5% of WideResNet's parameters, R2Net-S has 4.1% of ResNeXt-29's parameters, and R2Net-M has 23.4% of DenseNet-BC's parameters, yet they still achieve competitive accuracy. Note that R2Net effectively balances parameters and accuracy. These results demonstrate the effectiveness of R2GConv. Please refer to Appendix A.6 for details, and more results of R2Net with different groups (e.g., $\mathbf{C}_2$ / $\mathbf{C}_8$).

Instance Segmentation. Please refer to Appendix A.6 for detailed results and analysis.

4.3 VISUALIZATION

Visualization of RRE, SRE and NRE. The visualization of `RRE` (Ours), `SRE`, and Non-Rotation-Equivariance (`NRE`) is shown in Figure 5. We input (a) into R2Det-N (`RRE`), R2Det-N (`SRE`), and YOLOv8-N (`NRE`) to obtain the feature maps (b), (c), and (d), respectively. Observing the blue circles in (b), we notice slight differences but the overall feature maps are relaxed rotation-equivariant, showcasing the characteristic of our `RRE`. Observing the orange circles in (c), we find that the feature maps are strict rotation-equivariant, presenting `SRE`. Lastly, observing the red circles in (d), we find almost the characteristic of `NRE`. More visualizations can be found in Appendix A.7.

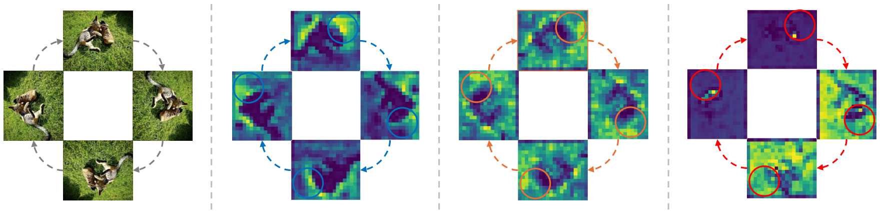
(a) Original images
(b) R2Det-N (RRE) feature maps
(c) R2Det-N (SRE) feature maps
(d) YOLOv8-N (NRE) feature maps

Figure 5: Visualization of the rotated feature maps in `RRE` (ours), `SRE`, and `NRE` based on $\mathbf{C}_4$.

Visualization of rotational Symmetry-Breaking. We also present a case of rotational symmetry-breaking on $\mathbf{C}_4$ in 2D object detection, as shown in Figure 6. We stretch a tvmonitor with $\mathbf{C}_4$ symmetry, therefore breaking its $\mathbf{C}_4$ symmetry. It can be seen that R2Det with `SRE` or `RRE` achieves similar detection probabilities in the unstretched image. However, in the stretched image, the detection probability decreased by 11% for R2Det with `SRE`, while R2Det with `RRE` only decreased by 3%. This example indicates that `RRE` can better model rotational Symmetry-Breaking situations.

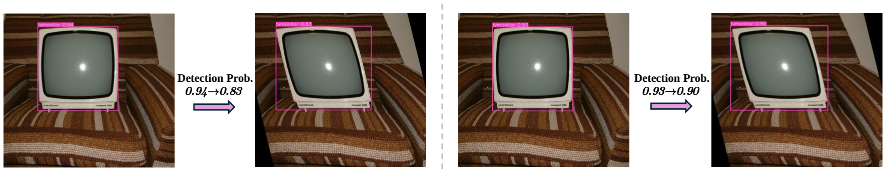

(a) R2Det-N with SRE
(b) R2Det-N with RRE (Ours)

Figure 6: An example of rotational Symmetry-Breaking on $\mathbf{C}_4$ in 2D object detection.

5 CONCLUSION

In this work, we propose a novel approach to build a `RRE` group $\mathbf{R}_n$ by perturbing a `SRE` group $\mathbf{C}_n$. Based on $\mathbf{R}_n$, we form a well-designed R2GConv operation, which tackles rotational Symmetry-Breaking situations to better align with real-world scenarios. Furthermore, we propose an efficient backbone R2Net and a redesigned 2D object detector named R2Det. Experiments demonstrate that our proposed R2Det achieves state-of-the-art performance compared to models without symmetry bias or with `SRE` constraints in 2D object detection. Additionally, R2Net as a feature extraction network can be extended to more complex visual tasks and scenes, leveraging the advantages of `RRE` by the proposed R2GConv operation.

REFERENCES

Michael M Bronstein, Joan Bruna, Taco Cohen, and Petar Veličković. Geometric deep learning: Grids, groups, graphs, geodesics, and gauges. *arXiv preprint arXiv:2104.13478*, 2021.

Nicolas Carion, Francisco Massa, Gabriel Synnaeve, Nicolas Usunier, Alexander Kirillov, and Sergey Zagoruyko. End-to-end object detection with transformers. In *European conference on computer vision*, pp. 213–229. Springer, 2020.

Alan F Chalmers. Curie's principle. *The British Journal for the Philosophy of Science*, 21(2): 133–148, 1970.

Wei Chen, Yan Li, Zijian Tian, and Fan Zhang. 2d and 3d object detection algorithms from images: A survey. *Array*, pp. 100305, 2023.

Taco Cohen and Max Welling. Group equivariant convolutional networks. In *International conference on machine learning*, pp. 2990–2999. PMLR, 2016a.

Taco S. Cohen and Max Welling. Steerable cnns. *CoRR*, abs/1612.08498, 2016b. URL `http://arxiv.org/abs/1612.08498`.

John Earman. Curie's principle and spontaneous symmetry breaking. *International Studies in the Philosophy of Science*, 18(2-3):173–198, 2004.

Gamaleldin F. Elsayed, Prajit Ramachandran, Jonathon Shlens, and Simon Kornblith. Revisiting spatial invariance with low-rank local connectivity. *CoRR*, abs/2002.02959, 2020. URL `https://arxiv.org/abs/2002.02959`.

Marc Finzi, Samuel Stanton, Pavel Izmailov, and Andrew Gordon Wilson. Generalizing convolutional neural networks for equivariance to lie groups on arbitrary continuous data. In *International Conference on Machine Learning*, pp. 3165–3176. PMLR, 2020.

Shang-Hua Gao, Ming-Ming Cheng, Kai Zhao, Xin-Yu Zhang, Ming-Hsuan Yang, and Philip Torr. Res2net: A new multi-scale backbone architecture. *IEEE Transactions on Pattern Analysis and Machine Intelligence*, 43(2):652–662, 2019.

Jan E Gerken, Jimmy Aronsson, Oscar Carlsson, Hampus Linander, Fredrik Ohlsson, Christoffer Petersson, and Daniel Persson. Geometric deep learning and equivariant neural networks. *Artificial Intelligence Review*, 56(12):14605–14662, 2023.

Ross Girshick, Jeff Donahue, Trevor Darrell, and Jitendra Malik. Rich feature hierarchies for accurate object detection and semantic segmentation. In *Proceedings of the IEEE conference on computer vision and pattern recognition*, pp. 580–587, 2014.

Jiaming Han, Jian Ding, Nan Xue, and Gui-Song Xia. Redet: A rotation-equivariant detector for aerial object detection. In *Proceedings of the IEEE/CVF conference on computer vision and pattern recognition*, pp. 2786–2795, 2021.

Kaiming He, Xiangyu Zhang, Shaoqing Ren, and Jian Sun. Delving deep into rectifiers: Surpassing human-level performance on imagenet classification. In *Proceedings of the IEEE international conference on computer vision*, pp. 1026–1034, 2015.

Kaiming He, Xiangyu Zhang, Shaoqing Ren, and Jian Sun. Deep residual learning for image recognition. In *Proceedings of the IEEE conference on computer vision and pattern recognition*, pp. 770–778, 2016.

Gao Huang, Zhuang Liu, Laurens Van Der Maaten, and Kilian Q Weinberger. Densely connected convolutional networks. In *Proceedings of the IEEE conference on computer vision and pattern recognition*, pp. 4700–4708, 2017.

Ningyuan Huang, Ron Levie, and Soledad Villar. Approximately equivariant graph networks. *Advances in Neural Information Processing Systems*, 36, 2024.

Muhammad Hussain. Yolo-v1 to yolo-v8, the rise of yolo and its complementary nature toward digital manufacturing and industrial defect detection. *Machines*, 11(7):677, 2023.

Peng-Tao Jiang, Chang-Bin Zhang, Qibin Hou, Ming-Ming Cheng, and Yunchao Wei. Layercam: Exploring hierarchical class activation maps for localization. *IEEE Transactions on Image Processing*, 30:5875–5888, 2021.

Glenn Jocher, Ayush Chaurasia, and Jing Qiu. Ultralytics YOLO, January 2023. URL `https://github.com/ultralytics/ultralytics`.

Sékou-Oumar Kaba and Siamak Ravanbakhsh. Symmetry breaking and equivariant neural networks. *arXiv preprint arXiv:2312.09016*, 2023.

Ravpreet Kaur and Sarbjeet Singh. A comprehensive review of object detection with deep learning. *Digital Signal Processing*, 132:103812, 2023.

Chanho Lee, Jinsu Son, Hyounguk Shon, Yunho Jeon, and Junmo Kim. Fred: Towards a full rotation-equivariance in aerial image object detection. In *Proceedings of the AAAI Conference on Artificial Intelligence*, volume 38, pp. 2883–2891, 2024.

Junying Li, Zichen Yang, Haifeng Liu, and Deng Cai. Deep rotation equivariant network. *Neurocomputing*, 290:26–33, 2018.

Wei Liu, Dragomir Anguelov, Dumitru Erhan, Christian Szegedy, Scott Reed, Cheng-Yang Fu, and Alexander C Berg. Ssd: Single shot multibox detector. In *Computer Vision–ECCV 2016: 14th European Conference, Amsterdam, The Netherlands, October 11–14, 2016, Proceedings, Part I 14*, pp. 21–37. Springer, 2016.

Francesco Locatello, Dirk Weissenborn, Thomas Unterthiner, Aravindh Mahendran, Georg Heigold, Jakob Uszkoreit, Alexey Dosovitskiy, and Thomas Kipf. Object-centric learning with slot attention. *Advances in Neural Information Processing Systems*, 33:11525–11538, 2020.

Diego Marcos, Michele Volpi, Nikos Komodakis, and Devis Tuia. Rotation equivariant vector field networks. In *Proceedings of the IEEE International Conference on Computer Vision*, pp. 5048–5057, 2017.

Joseph Redmon, Santosh Divvala, Ross Girshick, and Ali Farhadi. You only look once: Unified, real-time object detection. In *Proceedings of the IEEE conference on computer vision and pattern recognition*, pp. 779–788, 2016.

Tess E Smidt, Mario Geiger, and Benjamin Kurt Miller. Finding symmetry breaking order parameters with euclidean neural networks. *Physical Review Research*, 3(1):L012002, 2021.

Juan Terven, Diana-Margarita Córdova-Esparza, and Julio-Alejandro Romero-González. A comprehensive review of yolo architectures in computer vision: From yolov1 to yolov8 and yolo-nas. *Machine Learning and Knowledge Extraction*, 5(4):1680–1716, 2023.

Ao Wang, Hui Chen, Lihao Liu, Kai Chen, Zijia Lin, Jungong Han, and Guiguang Ding. YOLOv10: Real-Time End-to-End Object Detection. *arXiv e-prints*, art. arXiv:2405.14458, May 2024a.

Chien-Yao Wang, I-Hau Yeh, and Hong-Yuan Mark Liao. YOLOv9: Learning What You Want to Learn Using Programmable Gradient Information. *arXiv e-prints*, art. arXiv:2402.13616, February 2024b.

Rui Wang, Robin Walters, and Rose Yu. Approximately equivariant networks for imperfectly symmetric dynamics. In *International Conference on Machine Learning*, pp. 23078–23091. PMLR, 2022a.

Wenhai Wang, Enze Xie, Xiang Li, Deng-Ping Fan, Kaitao Song, Ding Liang, Tong Lu, Ping Luo, and Ling Shao. Pyramid vision transformer: A versatile backbone for dense prediction without convolutions. In *Proceedings of the IEEE/CVF international conference on computer vision*, pp. 568–578, 2021.

Wenhai Wang, Enze Xie, Xiang Li, Deng-Ping Fan, Kaitao Song, Ding Liang, Tong Lu, Ping Luo, and Ling Shao. Pvt v2: Improved baselines with pyramid vision transformer. *Computational Visual Media*, 8(3):415–424, 2022b.

Xihao Wang, Jiaming Lei, Hai Lan, Arafat Al-Jawari, and Xian Wei. Dueqnet: dual-equivariance network in outdoor 3d object detection for autonomous driving. In *2023 IEEE International Conference on Robotics and Automation (ICRA)*, pp. 6951–6957. IEEE, 2023.

Hermann Weyl. Symmetry. In *Symmetry*. Princeton University Press, 1952.

Saining Xie, Ross Girshick, Piotr Dollár, Zhuowen Tu, and Kaiming He. Aggregated residual transformations for deep neural networks. In *Proceedings of the IEEE conference on computer vision and pattern recognition*, pp. 1492–1500, 2017.

YuQing Xie and Tess Smidt. Equivariant symmetry breaking sets. *arXiv preprint arXiv:2402.02681*, 2024.

Sergey Zagoruyko and Nikos Komodakis. Wide residual networks. *arXiv preprint arXiv:1605.07146*, 2016.

Zhengxia Zou, Keyan Chen, Zhenwei Shi, Yuhong Guo, and Jieping Ye. Object detection in 20 years: A survey. *Proceedings of the IEEE*, 111(3):257–276, 2023.

A APPENDIX

A.1 MODEL ARCHITECTURE OF R2DET

In this section, we provide details of R2Det-N / S / M, as shown in Table 9.

Table 9: The parameter settings of R2Det-N / S / M. Among them, the **Index** column denotes the module index; the **From** column denotes where the input of this module comes from. For example, -1 denotes the upper module, $-1, 6$ denotes the upper module, and 6-module; the **OS** and **OC** columns denote the output size and channels from the upper module, respectively. In the **OC** column, n denotes the group order of our defined group $\mathbf{R}_n$. Note that the channel and size of the first input are 3 and 640×640, respectively.

Index	**From**	**Module**	**OS**	**R2Det-N**		**R2Det-S**		**R2Det-M**	
				OC	**Params.**	**OC**	**Params.**	**OC**	**Params.**
0	-1	Lifting R2GConv	320×320	$16n$	480	$32n$	944	48	1408
1	-1	Efficient R2GConv	160×160	$32n$	2416	$64n$	8912	$96n$	19504
2	-1	R2Net Block	160×160	$32n$	9640	$64n$	37680	$96n$	131152
3	-1	Efficient R2GConv	80×80	$64n$	8912	$128n$	34192	$192n$	75856
4	-1	R2Net Block	80×80	$64n$	58784	$128n$	232192	$192n$	409664
5	-1	Efficient R2GConv	40×40	$128n$	34192	$256n$	133904	$384n$	299152
6	-1	R2Net Block	40×40	$128n$	232192	$256n$	923072	$384n$	1630208
7	-1	Efficient R2GConv	20×20	$128n$	66960	$256n$	264976	$384n$	594064
8	-1	R2Net Block	20×20	$128n$	149056	$256n$	592992	$384n$	2072704
9	-1	R2SPPF	20×20	$128n$	65792	$256n$	262656	$384n$	590592
10	-1	Efficient R2GUp	40×40	$64n$	33040	$128n$	131600	$192n$	295696
11	-1, 6	Concat	40×40	$192n$	0	$384n$	0	$576n$	0
12	-1	R2Net Block	40×40	$128n$	181824	$256n$	724064	$384n$	2515072
13	-1	Efficient R2GUp	80×80	$64n$	33040	$128n$	131600	$192n$	295696
14	-1, 4	Concat	80×80	$128n$	0	$256n$	0	$384n$	0
15	-1	R2Net Block	80×80	$64n$	54064	$128n$	214592	$192n$	741472
16	-1	Efficient R2GConv	40×40	$64n$	17104	$128n$	66960	$192n$	149584
17	-1, 12	Concat	40×40	$192n$	0	$384n$	0	$576n$	0
18	-1	R2Net Block	40×40	$128n$	181824	$256n$	724064	$384n$	2515072
19	-1	Efficient R2GConv	20×20	$128n$	66960	$256n$	264976	$384n$	594064
20	-1, 9	Concat	20×20	$256n$	0	$512n$	0	$768n$	0
21	-1	R2Net Block	20×20	$256n$	592992	$512n$	2365600	$576n$	5320864
22	15	Transfer Block	80×80	$64n$	4288	128	16752	192	37408
23	18	Transfer Block	40×40	$128n$	16752	256	66256	384	148528
24	21	Transfer Block	20×20	$256n$	66256	512	263568	576	333376
25	22, 23, 24	v8Detect Head	-	-	897664	-	2147008	-	3822016
Total Params					**2.8M**		**9.6M**		**22.6M**
FLOPs					**4.0G**		**9.0G**		**17.3G**

A.2 DETAILED ARCHITECTURE OF R2DET AND R2NET.

R2Det leverages the outputs $\{\mathcal{O}_2, \mathcal{O}_3, \mathcal{O}_4\}$ from the last three stages of R2Net as inputs to fuse features across various scales and semantic levels, thereby allowing R2Det to detect objects of diverse sizes within an image. The output $\mathcal{O}_4$ is first refined by an R2SPPF designed for multi-scale spatial max pooling. Then $\mathcal{O}_2$, $\mathcal{O}_3$ and the refined $\mathcal{O}_4$ are fed into a standard FPN+PAN neck part, which includes R2Net Block, Efficient R2GConv, and Efficient R2GUp for 2× upsampling. Efficient R2GUp adopts the same architecture as Efficient R2GConv but uses the transposed convolution operation for upsampling during the depth-wise convolution stage. R2SPPF, similar to the architecture of R2Net Block, optimizes for parameter efficiency and enhances feature representation by capturing information at various scales. The obtained features $\{\widetilde{\mathcal{O}}_4, \widetilde{\mathcal{O}}_3, \widetilde{\mathcal{O}}_2\}$ are then input into Transfer Block for channel reduction, preparing for final detection by a universal v8Detector Head of YOLOv8. Transfer Block, which incorporates an Efficient R2GConv, ensures the features are appropriately shaped for the subsequent heads. v8Detector Head is an anchor-free approach for object's Bounding box (**Bbox**) and Classification (**Cls**) predictions, simplifying the prediction process.

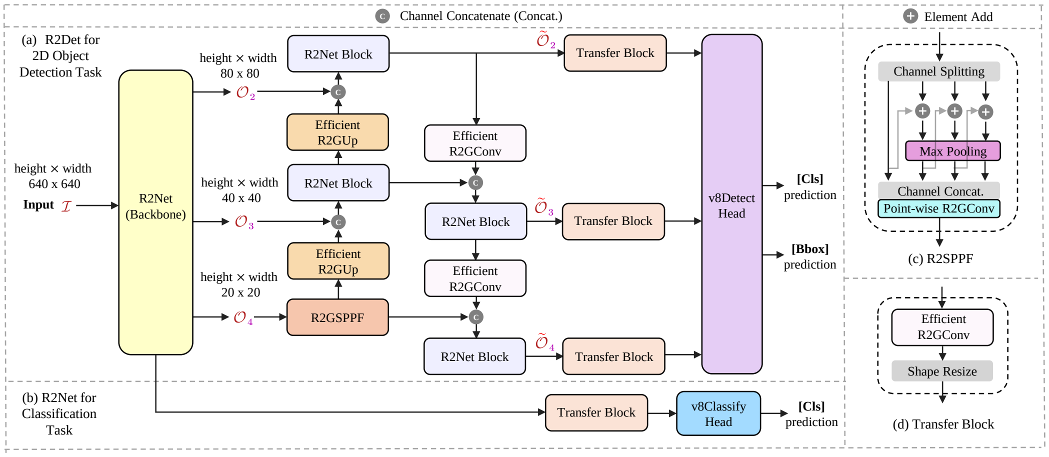

Figure 7: Detailed R2Det for 2D object detection task and R2Net for classification task.

A.3 HYPER-PARAMETER SETTINGS

The hyper-parameter settings of R2Det are shown in Table 10. R2Det employs the same hyper-parameter settings of YOLOv8 but only is trained in 300 epochs, which are less than YOLOv8's 500 epochs. And the hyper-parameter settings of R2Net are shown in Table 11.

Table 10: Hyper-parameter settings of R2Det.

Hyper parameter	**Value**
Epochs	300
Optimizer	SGD
Initial learning rate	0.01
Finish learning rate	0.0001
Learning rate decay	linear
Momentum	0.937
Weight decay	0.0005
Warm-up epochs	3
Warm-up momentum	0.8
Warm-up bias learning rate	0.1
Box loss gain	7.5
Class loss gain	7.5
DFL loss gain	1.5
HSV-Hue augmentation	0.015
HSV-Saturation augmentation	0.7
HSV-Value augmentation	0.4
Translation augmentation	0.1
Scale augmentation	0.5
Flip left-right augmentation	0.5
Mosaic augmentation	1.0
Close mosaic epochs	10

Table 11: Hyper-parameter settings of R2Net.

Hyper parameter	**Value**
Epochs	200
Optimizer	SGD
Initial learning rate	0.01
Finish learning rate	0.0001
Learning rate decay	linear
Momentum	0.937
Weight decay	0.0005
Warm-up epochs	3
Warm-up momentum	0.8
Warm-up bias learning rate	0.1
Class loss gain	7.5
HSV-Hue augmentation	0.015
HSV-Saturation augmentation	0.7
HSV-Value augmentation	0.4
Translation augmentation	0.1
Scale augmentation	0.5
Flip left-right augmentation	0.5
Mosaic augmentation	1.0
Close mosaic epochs	10

A.4 ANALYSIS ON THE LEARNABLE PERTURBATION PARAMETER Δ

The tendency of Δ is intrinsically linked to the degree of rotational Symmetry-Breaking within the system (or dataset). Here we further present the final Δ values, mean value, and variance from the first four layers of the full-trained Efficient R2GConv in the R2Det-N model in Table 12. Our R2Det has effectively integrated a rotational Symmetry-Breaking prior, with Δ in the proposed R2GConv capable of being updated end-to-end. These Δ values more accurately reflect rotational Symmetry-Breaking phenomena in natural datasets, i.e., a minor Relaxed Rotaion-Equivariance (`RRE`).

Table 12: The distribution of Δ values for four Efficient R2GConv in the full-trained R2Det-N on VOC training dataset. All of them are initialized from the Uniform distribution $\mathcal{U}(-0.1, 0.1)$.

No	Δ_1	Δ_2	Δ_3	Δ_4	**Mean value**	**Variance**
#1	$\begin{bmatrix} 0.0265 & -0.0041 \\ -0.0127 & 0.0325 \end{bmatrix}$	$\begin{bmatrix} 0.0310 & -0.0377 \\ 0.0284 & 0.0163 \end{bmatrix}$	$\begin{bmatrix} -0.0255 & 0.0114 \\ 0.0057 & -0.0343 \end{bmatrix}$	$\begin{bmatrix} 0.0072 & 0.0317 \\ -0.0310 & -0.0070 \end{bmatrix}$	0.0024	0.000624
#2	$\begin{bmatrix} -0.0063 & -0.1191 \\ -0.1504 & -0.1154 \end{bmatrix}$	$\begin{bmatrix} 0.1082 & 0.0729 \\ -0.0028 & -0.1312 \end{bmatrix}$	$\begin{bmatrix} 0.0629 & -0.0916 \\ -0.1335 & 0.0094 \end{bmatrix}$	$\begin{bmatrix} -0.1458 & 0.0432 \\ 0.0275 & 0.0356 \end{bmatrix}$	-0.0335	0.00812
#3	$\begin{bmatrix} -0.8716 & -0.0249 \\ 0.2800 & -0.0681 \end{bmatrix}$	$\begin{bmatrix} -0.4702 & 0.0441 \\ -0.2178 & 0.5107 \end{bmatrix}$	$\begin{bmatrix} 0.0856 & -0.5176 \\ -0.2120 & 0.1603 \end{bmatrix}$	$\begin{bmatrix} -0.5718 & -0.1320 \\ -0.1283 & -0.0665 \end{bmatrix}$	-0.138	0.119
#4	$\begin{bmatrix} -0.26733 & 0.32544 \\ 0.59473 & -0.4436 \end{bmatrix}$	$\begin{bmatrix} -0.21484 & -0.000070453 \\ -0.0061417 & -0.30835 \end{bmatrix}$	$\begin{bmatrix} 0.033966 & 0.44604 \\ 0.45483 & 0.42603 \end{bmatrix}$	$\begin{bmatrix} 0.45264 & -0.042358 \\ -0.15881 & 0.18347 \end{bmatrix}$	0.0922	0.106

A.5 ANALYSIS ON YOLOV8-N-CLS AND R2NET-N ON ROT-MINIST DATASET.

This section compares the training accuracy of YOLOv8-N-CLS and our R2Net-N on the ROT-MINIST dataset, as shown in the following Table. Note that our designed ROT-MINIST is different from standard Rotated MINST, which aims to test the robustness of our R2Net . Specifically, we manipulate the training set by randomly rotating $60,000$ images by 0, 90, 180, and 270 degrees while maintaining $10,000$ images unaltered in the test set to evaluate the performance of a model under rotation. In Figure 8, both R2Net-N and YOLOv8-N-CLS display fluctuations during training. However, R2Net-N exhibits milder fluctuations compared to the more pronounced oscillations observed in YOLOv8-N-CLS. This contrast highlights the superior rotation anti-interference capability of R2Net-N, which is primarily attributed to its novel Relaxed Rotation-Equivariance (`RRE`).

Table 13: Comparaison of the robustness of YOLOv8-N-CLS and R2Net-N ($\mathbf{C}_4$).

Method	**Dataset**	**Error**	**Params.**
YOLOv8-N-CLS	MINST ROT-MINIST	0.58 44.88	1.5M
R2Net-N ($\mathbf{C}_4$)	MINST ROT-MINIST	**0.54** **27.75**	0.8M

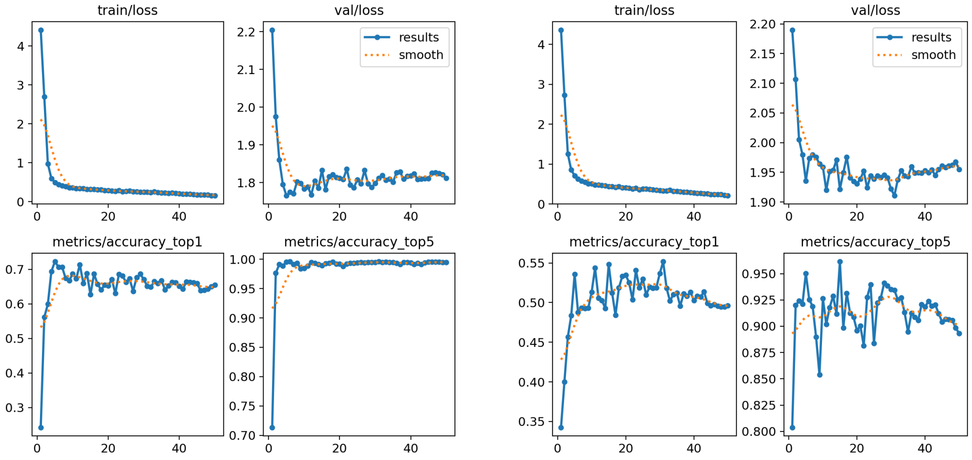

(a) R2Net-N

(b) YOLOv8-N-CLS

Figure 8: Comparison of YOLOv8-N and our R2Net-N in accuracy on ROT-MINST dataset. Both models are trained for 50 epochs with the resized input size 224×224 on dual 4090 GPUs .

A.6 ADDITIONAL EXPERIMENTS ON CLASSIFICATION AND INSTANCE SEGMENTATION

Classification. Also, we construct the backbone R2Net in three sizes (i.e., -N / S / M) on three groups (i.e., $\mathbf{C}_2$ / $\mathbf{C}_4$ / $\mathbf{C}_8$), incorporating the v8Classify Head for image classification, as shown in Figure 3. Table 8 shows the classification performance of our R2Net on CIFAR-10 / 100 datasets.

R2Net-M ($\mathbf{C}_2$) and R2Net-S ($\mathbf{C}_4$) both outperform other models in the accuracy of the CIFAR-10 dataset, but their parameters are much fewer. Also, R2Net-S ($\mathbf{C}_8$) and R2Net-M ($\mathbf{C}_8$) both exceed other models in accuracy of CIFAR-100 dataset. Still, they have fewer parameters compared to other models. We found that R2Net-S ($\mathbf{C}_4$) balances the parameter-accuracy trade-offs. These experiments show that R2Net still achieves excellent performance in natural classification tasks.

Table 14: Comparison of other models in top-1 accuracy (%) on CIFAR-10 / 100 datasets.

Method	**CIFAR-10** (%)	**CIFAR-100** (%)	**Params.**
WideResNet	95.8	79.5	36.5M
ResNeXt-29	96.4	82.7	68.1M
DenseNet-BC	96.5	82.8	25.6M
R2Net-N ($\mathbf{C}_2$)	94.3	77.4	0.6M
R2Net-S ($\mathbf{C}_2$)	95.9	79.5	1.7M
R2Net-M ($\mathbf{C}_2$)	96.7	80.5	3.4M
R2Net-N ($\mathbf{C}_4$)	95.8	80.6	0.9M
R2Net-S ($\mathbf{C}_4$)	96.6	82.2	2.8M
R2Net-M ($\mathbf{C}_4$)	97.3	82.7	6.0M
R2Net-N ($\mathbf{C}_8$)	96.2	81.5	1.4M
R2Net-S ($\mathbf{C}_8$)	96.9	83.6	5.0M
R2Net-M ($\mathbf{C}_8$)	**97.7**	**84.4**	11.2M

Table 15: Comparison of other models in instance segmentation on COCO-seg dataset.

Method	**Box AP**(%)	**Box AP**$_{50}$(%)	**Mask AP**(%)	**Mask AP**$_{50}$(%)	**Params.**	**FLOPs**
YOLOv8-N-seg	36.2	51.2	29.6	48.2	3.4M	12.6G
YOLOv8-S-seg	44.0	60.4	36.0	56.8	11.8M	42.6G
RTMDet-Ins-Tiny	40.5	-	35.4	-	5.6M	11.8G
RTMDet-Ins-S	44.0	-	38.7	-	10.2M	21.5G
R2Det-N-seg ($\mathbf{C}_4$)	43.7	59.3	35.8	56.2	3.0M	7.9G

- Note that R2Det-N-seg adopts the same architecture of R2Det-N but replaces *v8Detect Head* with *v8Segment Head*.

Instance Segmentation. We also conduct instance segmentation tasks on the COCO-seg dataset, as shown in Table 15. Compared to YOLOv8-N-seg, our R2Det-N-seg exhibits improvements of 20.7% in **Box AP** and 20.9% in **Mask AP**, with fewer parameters. R2Det-N-seg achieves similar **Mask AP** of YOLOv8-S-seg and RTMDet-Ins-Tiny, with only 25.4% and 53.6% of their parameters. Moreover, when compared to RTMDet-Ins-S, R2Det-N-seg has similar **Box AP** while utilizing only 29.4% parameters. The results show that our R2Det is also applicable to instance segmentation.

A.7 VISUALIZATION ANALYSIS ON RELAXED ROTATION-EQUIVARIANCE

In this subsection, we present a visualization of feature maps from our R2Det-N, as illustrated in Figure 9. We rotate the initial image (a) by 90, 180, and 270 degrees to generate images (b), (c), and (d) as inputs. It can be found that the output feature maps in (e), (f), (g), and (h), corresponding to each channel, exhibit consistency with minor variations, which demonstrates the Relaxed Rotation-Equivariance (`RRE`) property of our network.

A.8 HEATMAP VISUALIZATION

In this section, we present the visualization of LayerCAM (Jiang et al., 2021) heatmaps derived from YOLOv8-N, YOLOv7, YOLOv5, and our R2Det-N ($\mathbf{C}_4$), as depicted in Figure 10. These heatmaps enable us to locate the regions of interest where the network concentrates its attention. It can be seen that YOLOv7 and our R2Det-N achieved better feature focusing. Notably, R2Det-N shows a comprehensive focusing range on certain objects, such as dogs and zebras. In contrast, YOLOv8 and YOLOv5 fail to exhibit such targeted feature focus on these particular objects.

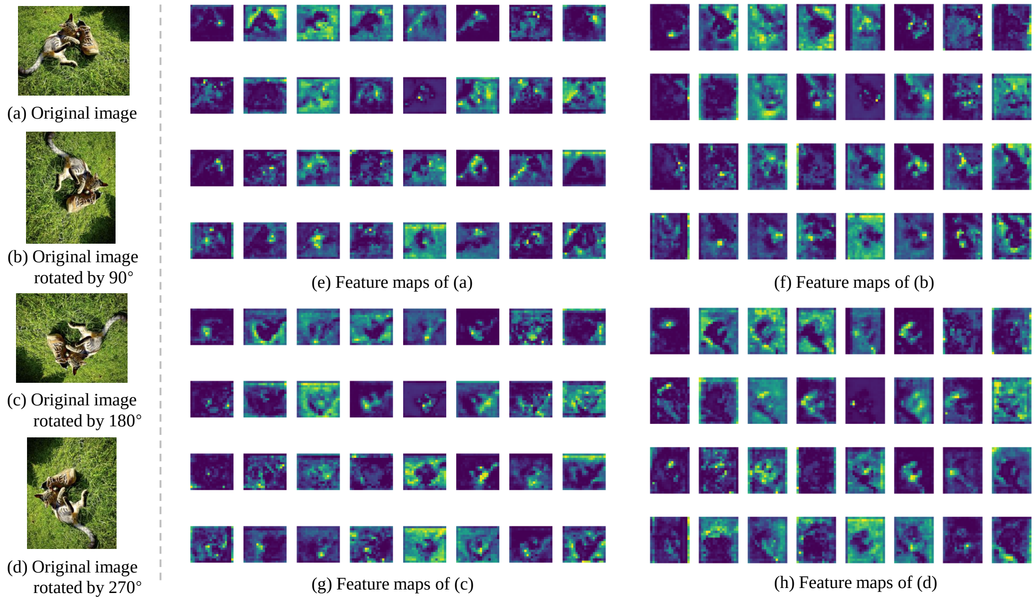
(a) Original image
(b) Original image rotated by 90°
(c) Original image rotated by 180°
(d) Original image rotated by 270°
(e) Feature maps of (a)
(f) Feature maps of (b)
(g) Feature maps of (c)
(h) Feature maps of (d)

Figure 9: The R2Det-N ($\mathbf{C}_4$) feature map visualization of the original image rotated at (a) 0, (b) 90, (c) 180, and (d) 270 degrees, as depicted in (e), (f), (g), and (h), corresponds to its 32 channels.

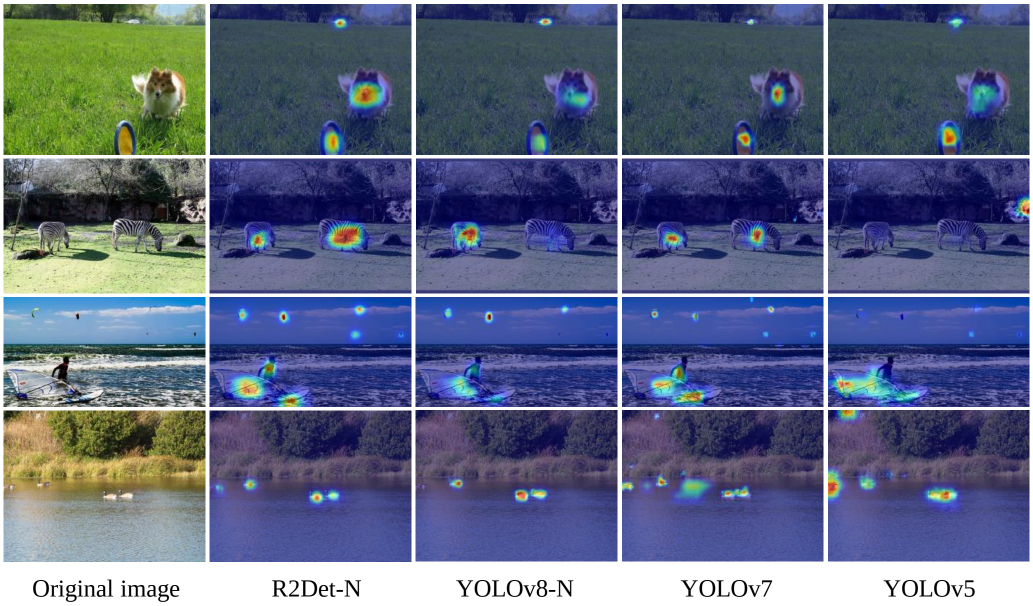

Figure 10: LayerCAM heatmaps visualizations of neck networks across YOLO (v8-N, v7, v5) and our R2Det-N ($\mathbf{C}_4$) models. Examples are from COCO dataset.

A.9 PARAMETER ANALYSIS OF EFFICIENT R2GCONV (OURS) AND GCONV ON $\mathbf{C}_n$

Assuming the input, output channels, and kernel size of both Efficient R2GConv and GConv are c_{in}, c_{out}, and k, respectively. The parameters of Efficient R2GConv can be calculated as follows:

$$c_{in} \times c_{out} \times n \times 1 \times 1\,(\textbf{Point-wise R2GConv}) + c_{out} \times 1 \times 1 \times k \times k\,(\textbf{Depth-wise R2GConv}) \\ + n \times 2 \times 2\,(\Delta) \approx n \times c_{in} \times c_{out} + k^2 \times c_{out}$$

where $\cdot$ in $(\cdot)$ denotes the source of parameters.

The parameters of GConv can be calculated as follows:

$$c_{in} \times c_{out} \times n \times k \times k = n \times c_{in} \times c_{out} \times k^2.$$

Therefore, the parameter of our Efficient R2GConv is only

$$\frac{n \times c_{in} \times c_{out} + k^2 \times c_{out}}{n \times c_{in} \times c_{out} \times k^2} = \frac{1}{k^2} + \frac{1}{n \times c_{in}}$$

of GConv.

A.10 PROOF OF GCONV (SRE) AND R2GCONV (RRE)

On $\mathbf{C}_n$ group, define $\mathbf{c}^i(\cdot)$ as rotation of $\cdot$ by $2\pi i/n$, and $\mathbf{c}^{i+1}(\cdot) = \mathbf{c}^{(i+1) \bmod n}(\cdot)$. We have the following conclusion (note that for simplicity, we ignore the input and output channels):

- **Conclusion 1.** $\mathbf{C}_n$-GConv (Vanilla Group Convolution) is a strict rotation-equivariant block.

  Proof. Given input x and initial weight ψ, we obtain the strict rotation-equivariant filter $\psi_i^{\text{strict}} = \mathbf{c}^i(\psi)$ in the i-order of $\mathbf{C}_n$. Then $\mathbf{C}_n$-GConv can be defined as: $f_1(x) = \sum_{i=0}^{n-1} x * \psi_i^{\text{strict}} = \sum_{i=0}^{n-1} x * \mathbf{c}^i(\psi)$. For any $j \in \{0, 1, \cdots, n-1\}$, we have

  - $f_1(\mathbf{c}^j(x)) = \sum_{i=0}^{n-1} \mathbf{c}^j(x) * \mathbf{c}^i(\psi)$
  - $\mathbf{c}^j(f_1(x)) = \mathbf{c}^j(\sum_{i=0}^{n-1} x * \mathbf{c}^i(\psi)) = \sum_{i=0}^{n-1} \mathbf{c}^j(x) * \mathbf{c}^{i+j}(\psi)$
    $= \sum_{i=0}^{n-1} \mathbf{c}^j(x) * \mathbf{c}^{(i+j) \bmod n}(\psi) = \sum_{i=0}^{n-1} \mathbf{c}^j(x) * \mathbf{c}^i(\psi)$.

  Therefore, $f_1(\mathbf{c}^j(x)) = \mathbf{c}^j(f_1(x))$. According to Eq. 1, complete the proof.

- **Conclusion 2.** $\mathbf{C}_n$-R2GConv (Ours) is a relaxed rotation-equivariant block.

  Proof. Given input x, initial weight ψ, an affine transformation function $\mathbf{t}$ and the learnable perturbation Δ, we obtain the relaxed rotation-equivariant filter $\psi_i^{\text{relaxed}} = \mathbf{t}^i(\psi, \Delta)$ in the i-order of $\mathbf{C}_n$. Then $\mathbf{C}_n$-R2GConv can be defined as: $f_2(x) = \sum_{i=0}^{n-1} x * \psi_i^{\text{relaxed}} = \sum_{i=0}^{n-1} x * \mathbf{t}^i(\psi, \Delta)$. For any $j \in \{0, 1, \cdots, n-1\}$, we have:

  - $f_2(\mathbf{c}^j(x)) = \sum_{i=0}^{n-1} \mathbf{c}^j(x) * \mathbf{t}^i(\psi, \Delta)$
  - $\mathbf{c}^j(f_2(x)) = \mathbf{c}^j(\sum_{i=0}^{n-1} x * \mathbf{t}^i(\psi, \Delta)) = \sum_{i=0}^{n-1} \mathbf{c}^j(x) * \mathbf{c}^j(\mathbf{t}^i(\psi, \Delta))$.

  Therefore, $||f_2(\mathbf{c}^j(x)) - \mathbf{c}^j(f_2(x))|| = ||\sum_{i=0}^{n-1} \mathbf{c}^j(x) * \mathbf{t}^i(\psi, \Delta) - \sum_{i=0}^{n-1} \mathbf{c}^j(x) * \mathbf{c}^j(\mathbf{t}^i(\psi, \Delta))|| = ||\sum_{i=0}^{n-1} \mathbf{c}^j(x) * (\mathbf{t}^i(\psi, \Delta) - \mathbf{c}^j(\mathbf{t}^i(\psi, \Delta)))|| \leq \epsilon$. According to Eq. 4, complete the proof.
  In particular, when $\Delta = 0$, we have $\mathbf{t}^i(\psi, \Delta) = \mathbf{c}^i(\psi)$, thus $||f_2(\mathbf{c}^j(x)) - \mathbf{c}^j(f_2(x))|| = 0$, i.e., $\epsilon = 0$, and f_2 is strict rotation-equivariant when $\Delta = 0$.

A.11 THEORETICAL ANALYSIS

Since the existing methods, including strict rotation-equivariant models, cannot perfectly tackle Symmetry-Breaking scenarios in object detection tasks, i.e., they can not learn a relaxed equivariant function. We assume from Wang et al. (2022a) that the ground truth function, named ϕ_{gt}, is relaxed equivariant. Firstly, we provide the Equivariance Error (EE), which quantifies how much the ground truth equivariant function ϕ_{gt} deviates from being strictly equivariant. The EE is defined as the maximum deviation from the strict-equivariant behavior under transformations, thereby illustrating how we can regulate the level of relaxation in the equivariance property.

Definition A.1 (*Equivariance Error*) *Let $\phi_{gt} : X \to Y$ be a function and G be a group. Assume that G acts on X and Y via $\rho_X : G \to \mathrm{GL}(X)$ and $\rho_Y : G \to \mathrm{GL}(Y)$. For any $g, \mathbf{x} \in G \times X$, the Equivariance Error of ϕ_{gt} is defined as follow:*

$$\|\phi_{gt}\|_{\mathrm{EE}} = \sup_{\mathbf{x}, g} \|\rho_Y(g) \cdot \phi_{gt}(\mathbf{x}) - \phi_{gt}(\rho_X(g) \cdot \mathbf{x})\|,$$

where $\|\cdot\|$ denote the `L2-Norm` operation. According to Equation 4 in the main text, the function ϕ_{gt} is relaxed (or ϵ-approximate) equivariant if and only if $\|\phi_{gt}\|_{\mathrm{EE}} \leq \epsilon$, where ϵ represents the maximum level of deviation from strict equivariance for ϕ_{gt} to be considered relaxed equivariant.

Next, we prove that if an input is close to its transformed version, the images under a continuous relaxed equivariant function still have to be close. This captures the idea of symmetry in the task, meaning that the output of the function is predictable under transformations of the input.

Proposition A.2 *Let ϕ_{gt} be relaxed (or ϵ-approximate) equivariant and Lipschitz with constant k. Then, we have*

$$\|\rho_Y(g) \cdot \phi_{gt}(\mathbf{x}) - \phi_{gt}(\mathbf{x})\| \leq k\|\rho_X(g) \cdot \mathbf{x} - \mathbf{x}\| + \epsilon, \quad \forall g, \mathbf{x} \in G \times X.$$

Proof. If ϕ_{gt} is Lipschitz with constant k, we have

$$\|\phi_{gt}(\rho_X(g) \cdot \mathbf{x}) - \phi_{gt}(\mathbf{x})\| \leq k\|\rho_X(g) \cdot \mathbf{x} - \mathbf{x}\|, \quad \forall g, \mathbf{x} \in G \times X.$$

Further, from the EE definition and triangle inequality, we have

$$\begin{aligned}\|\rho_Y(g) \cdot \phi_{gt}(\mathbf{x}) - \phi_{gt}(\mathbf{x})\| \leq & \|\rho_Y(g) \cdot \phi_{gt}(\mathbf{x}) - \phi_{gt}(\rho_X(g) \cdot \mathbf{x})\| \\ & + \|\phi_{gt}(\rho_X(g) \cdot \mathbf{x}) - \phi_{gt}(\mathbf{x})\| \\ \leq & k\|\rho_X(g) \cdot \mathbf{x} - \mathbf{x}\| + \epsilon, \quad \forall g, \mathbf{x} \in G \times X.\end{aligned}$$

□

Note that both terms, $k\|\rho_X(g) \cdot \mathbf{x} - \mathbf{x}\|$ and ϵ, collectively determine the overall upper limit of the equivariance error. The former term embodies the fundamental discrepancy inherently introduced by the specific transformation actions, which naturally exist in the real world and are random. Hence, in this work, we assume ρ as learnable permutations that can be modeled as variables Δ following a Uniform distribution, i.e., $\Delta \sim \mathcal{U}(-b, b)$. These learnable transformations are also inherently norm-conserving, thereby allowing us to incorporate ρ into our considerations implicitly. Consequently, when an input $\mathbf{x}$ exhibits proximity to its transformed version, the outputs under a continuously equivariant function will also maintain close. We further provide visualization experiments in Seciton 4.3 and Appendix A.7 as evidence. Moreover, ϕ_{gt} does not require maintaining all the symmetries of the input, in contrast to strict equivariance, which imposes constraints on the stabilizer of the output. Finally, since the model $\phi_{relaxed}$ aims to approximates ϕ_{gt}, the following proposition shows that the equivariance error of the $\phi_{relaxed}$ will converge to the $\|\phi_{gt}\|_{\mathrm{EE}}$.

Proposition A.3 *Let $\phi_{gt} \colon X \to Y$ be a function with $\|\phi_{gt}\|_{\mathrm{EE}} = \epsilon$. Assume $\|\phi_{gt} - \phi_{relaxed}\|_\infty \leq c$. Then $\|\rho_Y(g) \cdot \phi_{relaxed}(\mathbf{x}) - \phi_{relaxed}(\rho_X(g) \cdot \mathbf{x})\| \leq 2c + \epsilon$.*

Proof. By triangle inequality and invariance of the `L2-Norm`, we have

$$\begin{aligned}\|\rho_Y(g) \cdot \phi_{relaxed}(\mathbf{x}) - \phi_{relaxed}(\rho_X(g) \cdot \mathbf{x})\| \leq & \|\rho_Y(g) \cdot \phi_{relaxed}(\mathbf{x}) - \rho_Y(g) \cdot \phi_{gt}(\mathbf{x})\| \\ & + \|\rho_Y(g) \cdot \phi_{gt}(\mathbf{x}) - \phi_{gt}(\rho_X(g) \cdot \mathbf{x})\| \\ & + \|\phi_{gt}(\rho_X(g) \cdot \mathbf{x}) - \phi_{relaxed}(\rho_X(g) \cdot \mathbf{x})\| \\ \leq & c + \epsilon + c = 2c + \epsilon, \quad \forall g, \mathbf{x} \in G \times X.\end{aligned}$$

□

A.12 MORE COMPARISON OF STATE-OF-THE-ART OBJECT DETECTORS.

We also provide a more detailed comparison of state-of-the-art object detectors, e.g., YOLOv5, YOLOv6, YOLOv7, and Gold YOLO models, as shown in Table 17.

A.13 SUPPLYMENTAL EXPERIMENT DETAILS ON VOC TEST DATASET

Table 16 shows that **AP** for different 20 classes of the VOC test dataset are reported. Our R2Det demonstrates the overwhelming performance across various classes.

Table 16: Results of the VOC test dataset. The highest **AP**s for each class are indicated in **bold**.

Method	**AP of 20 classes**																				
	$\mathbf{AP}_{50}$	Aero	Bike	Bird	Boat	Bottle	Bus	Car	Cat	Chair	Cow	Table	Dog	Horse	Mbike	Person	Plant	Sheep	Sofa	Train	TV
Faster-RCNN	76.4	79.8	80.7	76.2	68.3	55.9	85.1	85.3	89.8	56.7	87.8	69.4	88.3	88.9	80.9	78.4	41.7	78.6	79 .8	85.3	72.0
R-FCN	80.5	79.9	87.2	81.5	72.0	69.8	86.8	88.5	89.8	67.0	88.1	74.5	89.8	90.6	79.9	81.2	53.7	81.8	81.5	85.9	79.9
SSD300	77.5	79.5	83.9	76.0	69.6	50.5	87.0	85.7	88.1	60.3	81.5	77.0	86.1	87.5	83.9	79.4	52.3	77.9	79.5	87.6	76.8
SSD512	79.5	84.8	85.1	81.5	73.0	57.8	87.8	88.3	87.4	63.5	85.4	73.2	86.2	86.7	83.9	82.5	55.6	81.7	79.0	86.6	80.0
DSSD321	78.6	81.9	84.9	80.5	68.4	53.9	85.6	86.2	88.9	61.1	83.5	78.7	86.7	88.7	86.7	79.7	51.7	78.0	80.9	87.2	79.4
DSSD513	81.5	86.6	86.2	82.6	74.9	62.5	89.0	88.7	88.8	65.2	87.0	78.7	88.2	89.0	87.5	83.7	51.1	86.3	81.6	85.7	83.7
YOLOv8-N	78.6	86.5	88.0	75.1	69.9	65.3	85.3	90.6	85.3	61.0	81.0	75.3	81.1	89.2	86.0	87.0	50.9	77.2	73.4	88.2	76.2
YOLOv8-S	81.6	90.7	89.1	80.2	72.8	69.4	89.0	92.3	88.1	63.5	85.3	75.6	84.9	92.1	89.9	88.4	55.1	80.9	77.0	89.4	79.2
YOLOv8-M	83.7	92.2	92.7	83.2	74.7	73.6	89.1	92.7	91.2	67.4	87.0	78.5	87.3	92.7	90.4	89.2	59.5	80.6	80.7	89.9	81.7
R2Det-M ($\mathbf{C}_4$)	84.1	92.4	90.7	85.1	78.0	74.1	89.4	92.7	90.1	67.9	86.2	79.8	88.0	93.0	89.4	90.2	58.1	84.7	78.9	89.3	83.3
R2Det-S ($\mathbf{C}_4$)	86.0	94.0	93.0	85.6	79.1	76.3	91.0	94.0	92.8	69.8	89.1	80.6	90.6	93.1	91.7	91.7	64.1	86.6	79.8	91.7	84.3
R2Det-M ($\mathbf{C}_4$)	**87.3**	**94.6**	**94.5**	**89.3**	**79.9**	**78.9**	**93.1**	**94.3**	**94.8**	**71.6**	**90.1**	**81.2**	**92.8**	**93.3**	**92.5**	**92.0**	**64.8**	**89.2**	**82.0**	**91.6**	**85.5**

Table 17: Comparison of state-of-the-art object detectors on the COCO validation dataset.

Method	$\mathbf{AP}_{50:95}(\%)$	$\mathbf{AP}_{50}(\%)$	$\mathbf{AP}_{75}(\%)$	$\mathbf{AP}_{S}(\%)$	$\mathbf{AP}_{M}(\%)$	$\mathbf{AP}_{L}(\%)$	**Params.**	**FLOPs**
YOLOv5u-N	34.3	49.7	37.2	16.8	38.1	48.4	2.6M	7.7G
YOLOv5u-S	43.1	59.9	47.2	24.7	47.6	58.4	9.1M	24.0G
YOLOv5u-M	49.1	66.0	53.8	31.2	54.2	65.4	25.1M	64.2G
YOLOv5u-L	52.3	69.2	57.2	34.8	57.9	69.1	53.2M	135.0G
YOLOv5u-X	53.3	70.2	58.2	36.9	58.9	69.3	97.2M	246.4G
YOLOv6-N v3.0	37.0	52.7	–	–	–	–	4.7M	11.4G
YOLOv6-S v3.0	44.3	61.2	–	–	–	–	18.5M	45.3G
YOLOv6-M v3.0	49.1	66.1	–	–	–	–	34.9M	85.8G
YOLOv6-L v3.0	51.8	69.2	–	–	–	–	59.6M	150.7G
YOLOv7	51.2	69.7	55.9	31.8	55.5	65.0	36.9M	104.7G
YOLOv7-X	52.9	71.1	51.4	36.9	57.7	68.6	71.3M	189.9G
YOLOv7-N AF	37.6	53.3	40.6	18.7	41.7	52.8	3.1M	8.7G
YOLOv7-S AF	45.1	61.8	48.9	25.7	50.2	61.2	11.0M	28.1G
YOLOv7 AF	53.0	70.2	57.5	35.8	58.7	68.9	43.6M	130.5G
YOLOv8-N	37.3	52.6	40.5	18.6	41.0	53.5	3.2M	8.7G
YOLOv8-S	44.9	61.8	48.7	26.0	49.9	61.1	11.2M	28.6G
YOLOv8-M	50.2	67.2	54.7	32.3	55.9	66.5	25.9M	78.9G
YOLOv8-L	52.9	69.8	57.5	35.3	58.3	69.8	43.7M	165.2G
YOLOv8-X	53.9	71.0	58.7	35.7	59.3	70.7	68.2M	257.8G
Gold YOLO-N	39.6	55.7	–	19.7	44.1	57.0	5.6M	12.1G
Gold YOLO-S	45.4	62.5	–	25.3	50.2	62.6	21.5M	46.0G
Gold YOLO-M	49.8	67.0	–	32.3	55.3	66.3	41.3M	87.5G
Gold YOLO-L	51.8	68.9	–	34.1	57.4	68.2	75.1M	151.7G
YOLO MS-N	43.4	60.4	47.6	23.7	48.3	60.3	4.5M	17.4G
YOLO MS-S	46.2	63.7	50.5	26.9	50.5	63.0	8.1M	31.2G
YOLO MS	51.0	68.6	55.7	33.1	56.1	66.5	22.2M	80.2G
GELAN-S	46.7	63.0	50.7	25.9	51.5	64.0	7.1M	26.4G
GELAN-M	51.1	67.9	55.7	33.6	56.4	67.3	20.0M	76.3G
GELAN-C	52.5	69.5	57.3	35.8	57.6	69.4	25.3M	102.1G
GELAN-E	55.0	71.9	60.0	38.0	60.6	70.9	57.3M	189.0G
YOLOv9-S	46.8	63.4	50.7	26.6	56.0	64.5	7.1M	26.4G
YOLOv9-M	51.4	68.1	56.1	33.6	57.0	68.0	20.0M	76.3G
YOLOv9-C	53.0	70.2	57.8	36.2	58.5	69.3	25.3M	102.1G
YOLOv9-E	55.6	72.8	60.6	40.2	61.0	71.4	57.3M	189.0G
YOLOv10-N	38.5	53.8	41.7	18.9	42.4	54.6	2.3M	6.7G
YOLOv10-S	46.3	63.0	50.4	26.9	51.1	63.7	7.2M	21.6G
YOLOv10-M	51.1	68.1	55.8	33.8	56.5	67.0	15.4M	59.1G
YOLOv10-B	52.5	69.6	57.2	35.1	57.8	68.4	19.1M	92.0G
YOLOv10-L	53.2	70.1	58.0	35.7	58.4	69.4	24.4M	120.3G
YOLOv10-X	54.4	71.4	59.4	37.1	59.9	71.1	29.5M	160.4G
$\mathbf{C}_4$-R2Det-N	43.7	59.5	47.8	24.2	48.2	59.3	2.8M	4.0G
$\mathbf{C}_4$-R2Det-S	50.0	66.5	54.6	30.5	55.7	66.2	9.6M	9.0G
$\mathbf{C}_4$-R2Det-M	53.1	70.3	57.9	36.4	58.7	69.6	22.6M	17.3G